Available online at www.sciencedirect.com
ScienceDirect
Comput. Methods Appl. Mech. Engrg. 373 (2021) 113554
Computer methods in applied mechanics and engineering
www.elsevier.com/locate/cma

Comparison of fully-coupled and sequential solution methodologies for enhanced geothermal systems

Bruce Gee, Robert Gracie*

Department of Civil and Environmental Engineering, University of Waterloo, Waterloo, Ontario N2L 3G1, Canada

Received 29 May 2020; received in revised form 27 October 2020; accepted 29 October 2020
Available online 19 November 2020

Abstract

The simulation of enhanced geothermal systems (EGS) requires finding the solution to a highly coupled nonlinear set of partial differential equations. Verification of EGS modelling has been difficult due to a lack of analytical or semi-analytical solutions and is typically limited to a subset of processes. A comparison of alternative solution schemes is one method to numerically verify the coupling between all processes simultaneously and provide confidence in the solutions produced by the different solution schemes. This article presents the first such comparison of monolithic and sequential solution schemes for the modelling of EGS wells. A custom thermo-hydro-mechanical finite element model for an EGS well connected by planar fractures is developed along with two monolithic schemes; one using the Newton–Raphson iterative method and another using the Newton–Raphson iterative method modified by Aitken's Δ^2 relaxation method. The two monolithic schemes are compared against two sequential schemes and one loosely-coupled scheme in terms of accuracy and computational efficiency. The monolithic schemes are shown to have an optimal rate of convergence with respect to mesh and timestep refinement. The monolithic Newton–Raphson scheme is shown to require small timesteps that violate the minimum timestep size of the β-method of time integration, introducing spurious oscillations into the solution. Aitken's Δ^2 relaxation method is shown to improve the ability of the Newton–Raphson scheme to find a converged solution at larger timesteps, avoiding spurious oscillations and reducing overall computation time. The sequential solution schemes are shown to provide optimal rates of convergence with respect to mesh and timestep refinement and converge to the same solution as the monolithic solution schemes, verifying the results of both methodologies and previous modelling efforts. It is demonstrated that the sequential solution schemes are computationally more expensive than the monolithic schemes when seeking well-converged solutions. The loosely-coupled scheme demonstrates an optimal rate of convergence with mesh and timestep refinement, but is also shown to be much less accurate than the other schemes. The recommended solution scheme for the efficient simulation of EGSs is thus the Newton–Raphson scheme with Aitken's Δ^2 relaxation.

Keywords: Enhanced geothermal; Coupling; Verification

1. Introduction

Geothermal power is a largely untapped renewable energy source generated by radioactive decay within the Earth's crust. Deep geothermal refers to the energy stored within high temperature rock masses available at depths

* Corresponding author.
E-mail addresses: b3gee@uwaterloo.ca (B. Gee), rgracie@uwaterloo.ca (R. Gracie).

https://doi.org/10.1016/j.cma.2020.113554
0045-7825/

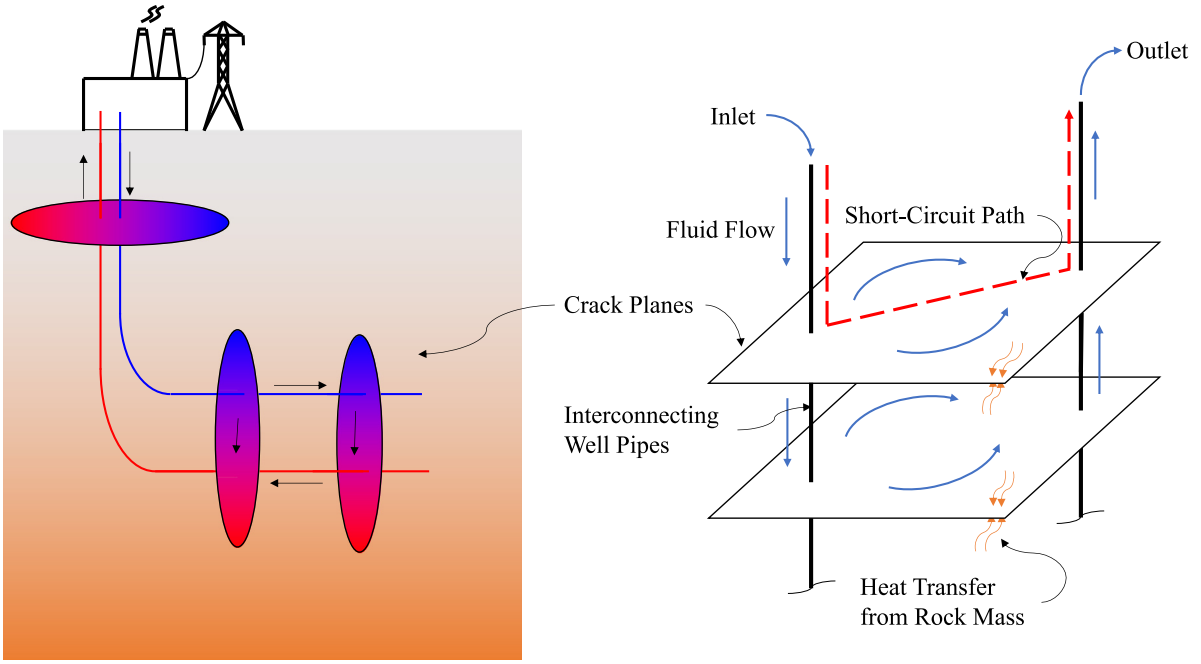

Fig. 1. Schematic of an enhanced geothermal doublet well. The image on the left shows the orientation of the system relative to the surface, while the image on the right shows a close-up schematic of the system and the fluid flow within the system.

beyond 1 km. Extracting the heat from these deep rock formations has been difficult since it traditionally requires a rock mass that is both hot and naturally porous [1]. However, Enhanced Geothermal Systems (EGS), also called Hot Dry Rock (HDR) installations, provide new opportunities to access this energy. In an EGS installation, the permeability of a hot rock mass is enhanced through the use of hydraulic fracturing, creating a fracture network through which fluid can flow. The long-term viability of EGS wells as a reliable energy source can be sabotaged by the coupled thermo-hydro-mechanical process known as flow channelling — a positive feedback loop in which the aperture of a cooling fracture increases, drawing fluid towards the already-cooled regions of the reservoir, and away from the hot areas of the reservoir [2]. Fig. 1 shows a diagram of an EGS doublet well (one injection and one production well) in which the wells are hydraulically connected by large planar fractures. The fracture planes develop normal to the direction of the minimum in-situ stress, and so fracture planes are oriented horizontally in shallower reservoirs and vertically in deeper reservoirs.

There are many processes within a geothermal reservoir that interact with each other, posing unique modelling challenges for the system. This model focuses on the following four processes: heat transfer in the rock mass, heat transfer within the fluid, fluid flow through the rock mass, and deformation of the rock mass. The primary challenge from a numerical methods perspective is then how to obtain accurate approximate solutions to the coupled set of nonlinear partial differential equations that govern these processes.

Existing modelling works can be categorized according to their fluid flow models: continuum flow, network flow, or dominant fracture flow. The first type of flow model, continuum flow, idealizes the fractured rock mass as a porous continuum through which the fluid flows. These continuum models generally apply to geothermal systems in porous rock formations and have been used to investigate: poro-thermal coupled effects, such as in the works of Zeng et al. [3], Aliyu and Chen [4], and Wang et al. [5]; and poro-thermo-mechanical coupled behaviour by Ghassemi and Zhou [6] and Gan and Elsworth [7]. The second type of flow model, network flow, assumes the injection and production wells are connected using a discrete fracture network. These fracture networks are typically randomly generated since the actual fracture networks are unknown. These models have been investigated for hydro-thermal effects by Shaik et al. [8], Chen et al. [9], Vasilyeva et al. [10,11], and HosseiniMehr, Vuik, and Hajibeygi [12]; and thermo-hydro-mechanical effects by Wang et al. [13], Zhang et al. [14], and Garipov and Hui [15]. The last typical flow model is dominant fracture flow, in which flow between the injection and production

well is restricted to some number of discrete dominant fracture planes. This flow model has much in common with network flow models but brings greater intention to the abstraction and simplifies the network of fractures to a few dominant fracture planes. The rock masses may be permeable or naturally fractured, but fluid flow outside the dominant fractures is typically assumed to be negligible. The dominant fracture planes may be an abstraction of several linked non-planar fractures which form a dominant flow pathway through the rock mass, but the tortuosity of the linked fractures is not considered. The advantage of such models is that they are computationally tractable while including the important physics of flow in the fractures. This is the assumed geometry for the EGS modelling in this paper. Single fracture plane systems have been investigated in terms of hydro-thermal behaviour by Mohais et al. [16] and Xia et al. [17]; and thermo-hydro-mechanical behaviour by Guo et al. [18], Pandey et al. [19], and Salimzadeh et al. [20]. Multi-fracture plane systems have been investigated for purely hydrological behaviour by Asai et al. [21]; hydro-thermal behaviour by Han et al. [22] and Gong et al. [23]; and thermo-hydro-mechanical behaviour by Slatlem Vik et al. [24]. Dominant fracture flow models have also been extended to investigate the effects of coupled fracture and low-permeability porous continuum flow by Salimzadeh, Nick, and Zimmerman [25], and the effects of chemical dissolution of the rock mass by Salimzadeh and Nick [26].

Despite a large number of applications, relatively little has been done to advance the verification of the numerical models used. Numerical approximations of the nonlinear set of coupled partial differential equations may be performed monolithically or sequentially. In a sequential scheme, the governing equations are solved in a staggered fashion one-by-one, by making assumptions about the other processes as each equation is solved. Ideally, though not always in practice, the sequential solution scheme is then iterated until convergence of all equations is achieved. A loosely-coupled scheme is a type of staggered scheme in which no iteration is performed after solving the equations, and thus is also known as a one-pass scheme. In a monolithic scheme, also known as a fully-coupled scheme, the governing equations are solved simultaneously. Monolithic schemes for coupled systems are typically expected to have the highest rate of convergence, but sequentially coupled schemes are often preferable. Solving a coupled problem using a monolithic scheme involves the development of a unique solver specific to the coupled problem under consideration. By contrast, sequential schemes can make use of pre-existing solvers for individual processes/partial differential equations within the system. Sequential schemes arise naturally when joining pre-existing solvers, and thus are common amongst commercial multiphysics software. A complete list of commercial multiphysics software used in EGS well modelling is provided by [2]. In the context of EGS simulation, examples of implementation of monolithic schemes are rare or non-existent, while sequential schemes are the standard. Case in point, all of the aforementioned coupled models are based on sequential schemes. Furthermore, there does not seem to be any examples in which the results of one sequential scheme are verified against an alternative sequential solution or a monolithic solution.

Verification of solution strategies is important to ensure model robustness, stability, and reliability. Even iterating until a converged solution is achieved, sequential solution schemes can be unreliable. The issues with sequential solution schemes are well documented in the field of hydraulic fracturing, in which sequentially coupled systems may develop spurious oscillations or fail to converge in many practical problems [27,28]. In the context of hydraulic fracturing, monolithic schemes are more robust and show higher convergence rates. Analogous problems have also been observed in poromechanical models involving simple sequential schemes, which has lead to the development of the undrained and fixed-stress splits [29–31]. To date, verification of sequentially coupled simulators for EGS modelling has been incomplete. Verification has been hindered by a lack of analytical or semi-analytical solutions stemming from the non-linear and coupled nature of the partial differential equations in EGS modelling. It is possible, and common, to verify the solver for each individual process on its own, or to verify the coupling between a subset of two processes. In practice, it is very difficult to verify that the coupling between all fields simultaneously is producing appropriate results. A comparison between monolithic and sequential schemes in terms of results and convergence is one method to verify the methodologies and implementation, and provide confidence to the results produced by both schemes. Until now, no such study of sequential and fully-coupled schemes with respect to EGS modelling has been available in the literature.

This paper seeks to address the gap in the verification of EGS modelling and provides confidence to the results of previous modelling efforts, while at the same time providing insights into the relative efficiency and accuracy of the various schemes available for solving the coupled system of equations. A unique thermo-hydro-mechanical finite element model is developed and implemented for enhanced geothermal well systems consisting of one or more injection wells hydraulically connected to one or more production wells by one or more discrete

fracture planes. Two fully-coupled monolithic solution schemes are developed, the first being a Newton–Raphson iterative scheme and the second being a Newton–Raphson scheme modified by Aitken's Δ^2 relaxation method. The fully-coupled schemes are compared against two sequential schemes: one in which the thermal subproblem is decoupled from the mechanical subproblem; and another in which the thermal, fluid flow, and deformation subproblems are all decoupled. The fully-coupled and sequential schemes are also compared against a one-pass loosely-coupled solution scheme. The performance of these five algorithms is studied with respect to convergence rates, accuracy, robustness, and computational efficiency. In the following section, a detailed description of the mathematical model, boundary conditions, and discretization is provided. In Section 3, five different solution algorithms to solve the coupled system are developed and discussed. In Section 4, a numerical convergence study is performed to compare the behaviour of the different solution algorithms. Section 5 discusses the behaviour of the different solution algorithms by examining the predicted results for an EGS doublet well system connected by a single fracture plane, and an EGS doublet well system connected by two fracture planes. Lastly, Section 6 summarizes the findings and conclusions.

2. Mathematical model

This section describes the mathematical model developed for an enhanced geothermal well consisting of one or more injection wells and one or more production wells connected by one or more fracture planes. It first details the governing equations and boundary conditions, then discusses the discretization using the finite element method.

The following modelling assumptions are made:

1. There are four processes of interest: heat transfer in the solid, heat transfer in the fluid, fluid flow within the fractures, and deformation of the rock mass.
2. The heat transfer in the rock mass is transient and the deformation of the rock mass is quasi-static. The transient effects of fluid flow and heat transfer in the fluid are assumed to dissipate quickly relative to the timescale of interest, such that the processes are considered quasi-steady-state.
3. The porosity of the rock mass is very low, such that fluid flow is restricted to discrete fracture planes and well pipes. These fracture planes have been created prior to and independent of the heat extraction process, i.e., by previous hydraulic fracturing. There is no interaction between the well pipes and the rock mass.
4. The fluid within the fractures is incompressible and Newtonian.
5. The fractures are initially closed at the beginning of the well's life, but may have a small initial effective aperture.

2.1. Governing equations and boundary conditions

Consider a solid domain, Ω, which contains some number of discrete fractures, Γ_c, as illustrated in Fig. 2. There are four fields that exist within the domain: the solid displacement field, $\boldsymbol{u} \in \Omega$ [m], the solid temperature field, $\theta \in \Omega$ [°C], the fluid pressure field, $p \in \Gamma_c$ [Pa], and the fluid temperature field, $T \in \Gamma_c$ [°C].

The solid domain is bounded by a boundary, Γ. The solid displacement field boundary is subdivided such that $\Gamma = \Gamma_u \cup \Gamma_t \cup \Gamma_c$ and $\Gamma_u \cap (\Gamma_t \cup \Gamma_c) = \emptyset$. Γ_u represents the Dirichlet boundary of the domain, Γ_t represent the Neumann boundary of the domain, and Γ_c represents the internal crack boundary. Γ_c^+ and Γ_c^- represent the positive and negative faces of the internal crack boundary.

The displacement of the rock mass, $\boldsymbol{u}$, is governed by the equilibrium equation:

$$\nabla \cdot \boldsymbol{\sigma}(\boldsymbol{u}) + \rho_s \boldsymbol{g} = 0 \tag{1}$$

in which $\boldsymbol{\sigma}$ [Pa] is the total Cauchy stress tensor, ρ_s [kg/m^3] is the density of the solid rock mass, and $\boldsymbol{g}$ [m/s^2], is the vector of accelerations due to gravity. The domain is assumed to be under an in-situ stress field, $\boldsymbol{\sigma}_0$, which is in equilibrium with gravity. Assuming linear thermoelasticity, the constitutive equation relating stress and strain in the rock mass is

$$\boldsymbol{\sigma} - \boldsymbol{\sigma}_0 = \mathbb{C} : (\boldsymbol{\varepsilon} - \boldsymbol{\varepsilon}_\theta) \tag{2}$$

$$\boldsymbol{\varepsilon}_\theta = \alpha \Delta\theta \mathbf{I} \tag{3}$$

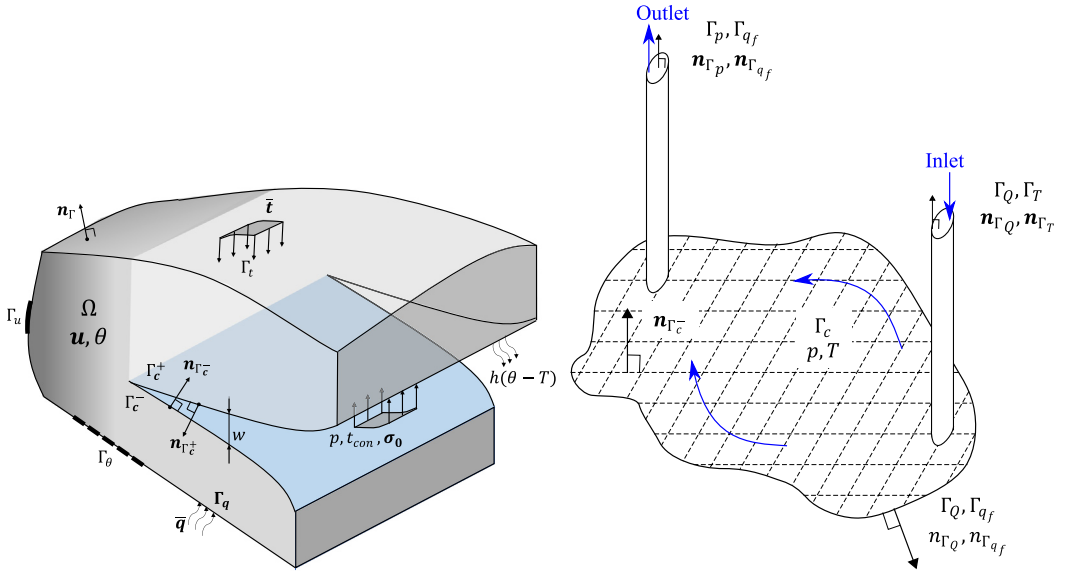

Fig. 2. Illustration of mathematical domains and boundaries. The image on the left shows the solid domain, Ω, and its boundaries, $\Gamma_c, \Gamma_u, \Gamma_t \Gamma_\theta, \Gamma_q$. The image on the right shows the fluid domain, Ω_f / Γ_c, and its boundaries $\Gamma_p, \Gamma_Q, \Gamma_T, \Gamma_{q_f}$.

in which $\mathbb{C}$ [Pa] is the 4th order linear elasticity tensor, $\boldsymbol{\varepsilon}_\theta$ is the thermal strain, α [m/m °C] is the coefficient of linear thermal expansion, and $\Delta\theta = \theta - \theta_0$ is the difference between the current and initial rock mass temperature, θ_0. The linear strain tensor is defined as

$$\boldsymbol{\varepsilon} = \frac{1}{2}(\nabla \boldsymbol{u} + \nabla \boldsymbol{u}^\top) \tag{4}$$

Contact across the fractures is enforced using a penalty method. The contact traction, $\bar{t}_{con}$ [Pa], is assumed to be a linear function of the fracture aperture such that

$$\bar{t}_{con} = \begin{cases} k_{con} w & \text{if } w \leq 0 \\ 0 & \text{if } w > 0 \end{cases} \tag{5}$$

in which k_{con} [Pa/m] is a contact stiffness and w [m] is the fracture aperture.

The solid temperature field, θ, is governed by conservation of energy. Heat conduction within the solid rock mass is slow compared to the other modelled processes. Therefore, heat transfer in the rock mass is considered as transient. As the rate of deformation is slow, thermoelastic dissipation is negligible and the uncoupled quasi-static thermoelastic formulation is used such that there is a one-way coupling between the temperature and deformation of the rock mass. Neglecting body sources, the conservation of energy within the rock mass is given by

$$\rho_s c_{ps} \dot{\theta} = \nabla \cdot (-k_s \nabla \theta) \tag{6}$$

in which c_{ps} [J/kg °C] is the specific heat of the solid rock mass, and k_s [W/m °C] is the thermal conductivity of the solid domain. Heat transfer between the rock mass and fluid in the fractures is incorporated through boundary conditions acting on the internal fracture surfaces, which is discussed below.

In an EGS reservoir, permeability of the rock mass is very low. For example, the permeability of the rock mass at Utah FORGE geothermal exploration site is on the order of $10^{-20} - 10^{-21}$ m^2 [32]. The fractures therefore form the dominant flow pathway through the rock mass and the flow through the rock matrix is negligible. The rock mass is therefore assumed to be impermeable, and the fluid domain, Ω_f, is equivalent to the crack boundary, Γ_c. The Dirichlet and Neumann boundaries of the fluid pressure field are denoted as Γ_p and Γ_Q respectively. The Dirichlet and Neumann boundaries of the fluid temperature field are denoted as Γ_T and Γ_{q_f} respectively. In this way, the fracture planes are modelled one dimension lower than the rock mass, and thus the modelled velocity $\boldsymbol{v}$, and fluid temperature, T, represent the average values across the fracture aperture. Fig. 3 shows the modelled averages of

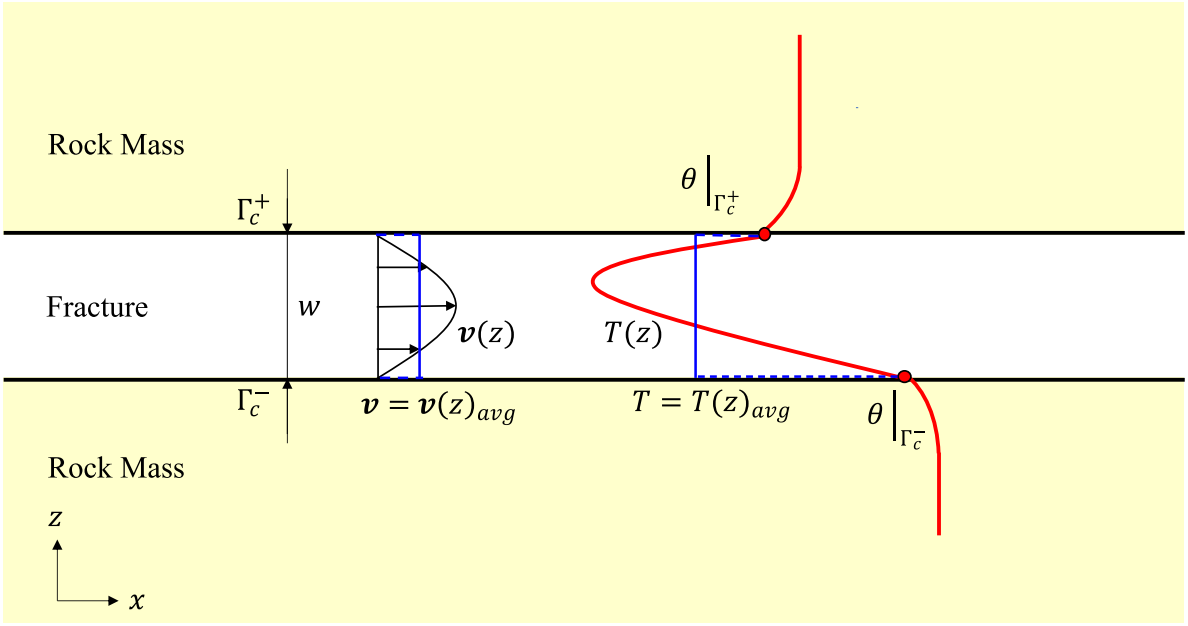

Fig. 3. Illustration of the distribution of temperature and velocity across the fracture aperture, $T(z)$ and $\boldsymbol{v}(z)$, compared with the modelled distributions, T and $\boldsymbol{v}$. T and $\boldsymbol{v}$ represent the average values of the true distributions across the aperture.

fluid flow and temperature within the fracture planes compared to their true distributions. The use of average fluid quantities means that in general, a jump in the temperature field occurs between the fluid and solid at the crack surface.

The fluid flow within the fractures is governed by conservation of fluid mass and is assumed to be steady. The fluid is assumed to be incompressible and Newtonian. The only sources and sinks of fluid mass within the fractures are the injection and production wells. The inlet and outlet pipes are treated as point sources within the fracture. The conservation of fluid mass is given as

$$\nabla \cdot (\rho_f \boldsymbol{q}) = q_{pi}\delta(\mathbf{X}_{in}) - q_{po}\delta(\mathbf{X}_{out}) \tag{7}$$

in which $\boldsymbol{q}$ [m^2/s] is the fluid flux, and ρ_f [kg/m^3] is the density of the fluid, q_{pi} and q_{po} [kg/s] are the fluid fluxes from the injection and production wells respectively, and $\delta(\mathbf{X})$ [m^{-2}] is the Dirac delta function evaluated at the inlet and outlet positions, $\mathbf{X}_{in}$ and $\mathbf{X}_{out}$. It is assumed that there is no leakoff of fluid mass since the flow is quasi-steady, such that all the fluid enters the domain via the injection wells and leaves via the production wells. The fracture aperture is assumed to be small such that the flow is laminar. Neglecting entrance/exit effects, the fluid flux is assumed to be given by Poiseuille flow:

$$\boldsymbol{q} = w\boldsymbol{v} = wk(\nabla p - \rho_f \boldsymbol{g}) \quad \text{with} \quad k = k(w) = \frac{w^2}{12\mu} \tag{8}$$

in which w [m] is the fracture aperture, $\boldsymbol{v}$ [m/s] is the average fluid velocity, μ [Pa s] is the dynamic viscosity of the fluid, and k [m^2/Pa s] is the permeability of the fracture. The aperture of the crack is defined as

$$w = w_0 + w(\mathbf{u}) \tag{9}$$

in which w_0 is an initial effective crack aperture, and $w(\mathbf{u})$ is the change in aperture due to thermo-mechanical deformation.

Crack planes are hydraulically connected to the surface and to each other by the injection and production wells, which are modelled as pipes. Fluid flow within the pipes is assumed to be laminar and steady. The pipes are modelled as one-dimensional and do not interact with the rock mass. The conservation of mass and fluid flux

within the one-dimensional pipes are given as

$$0 = \frac{\partial}{\partial s}(\rho_f q) \tag{10}$$

$$q_p = k(\frac{\partial}{\partial s} p - \rho_f \boldsymbol{g} \cdot \mathbf{n}_s) \quad \text{with} \quad k = \frac{\pi D^4}{128 \mu L_P} \tag{11}$$

in which D [m] is the pipe diameter, and L_P [m] is the pipe length, s [m] is the local spatial coordinate of the well pipe, and $\mathbf{n}_s$ is the tangent vector to the local spatial coordinate s.

The average fluid temperature field, T, is governed by conservation of energy. In-plane heat transfer occurs due to conduction between fluid particles, and advection of the bulk fluid. The fluid interacts with the solid temperature field on both sides of the crack, Γ_c, through convection. Heat transfer is advection dominant in applications of practical concern, and so the average temperature of the fluid changes very quickly compared to changes in the temperature of the rock mass crack surfaces. Thus the heat transfer in the fluid is modelled as a quasi-steady-state process. The rate of heat transfer between the solid and fluid temperatures is governed by convection, such that the rate of heat transfer is proportional to the difference between temperatures of the crack surface and the mean temperature of the fluid. These conditions appear as a boundary condition on conservation of energy in the rock mass (6), and as a body source term within conservation of energy in the fluid. Conservation of energy in the fluid is given as

$$\nabla \cdot \left(-k_f w \nabla T\right) + \rho_f c_{pf} w \boldsymbol{v} \cdot \nabla T - h \left[(\theta|_{\Gamma_c^+} - T) + (\theta|_{\Gamma_c^-} - T)\right] = 0 \tag{12}$$

in which k_f [W/m °C] is the thermal conductivity of the fluid, c_{pf} [J/kg °C] is the specific heat of the fluid, and h [W/m^2 °C] is the heat transfer coefficient between the fluid and the solid. The heat transfer coefficient is determined using the Nusselt number, Nu [–], which is a constant on the order of 10^0 for fully developed laminar flow within a duct [33]. The Nusselt number is given by $Nu = 2whk_f^{-1}$, such that the heat transfer coefficient is a function of the crack aperture, $h = h(w^{-1})$.

The boundary conditions on the solid rock mass are

$$\boldsymbol{u} = \overline{\boldsymbol{u}} \quad \text{on } \Gamma_u \tag{13}$$

$$\theta = \overline{\theta} \quad \text{on } \Gamma_\theta \tag{14}$$

$$\boldsymbol{\sigma} \cdot \mathbf{n}_{\Gamma_c^+} = (-p\mathbf{I} + \boldsymbol{\sigma}_0 - \overline{t}_{con}\mathbf{I}) \cdot \mathbf{n}_{\Gamma_c^+} \quad \text{on } \Gamma_c^+ \tag{15}$$

$$\boldsymbol{\sigma} \cdot \mathbf{n}_{\Gamma_c^-} = (-p\mathbf{I} + \boldsymbol{\sigma}_0 - \overline{t}_{con}\mathbf{I}) \cdot \mathbf{n}_{\Gamma_c^-} \quad \text{on } \Gamma_c^- \tag{16}$$

$$-k_s \nabla\theta \cdot \mathbf{n}_{\Gamma_c^+} = h(\theta|_{\Gamma_c^+} - T) \quad \text{on } \Gamma_c^+ \tag{17}$$

$$-k_s \nabla\theta \cdot \mathbf{n}_{\Gamma_c^-} = h(\theta|_{\Gamma_c^-} - T) \quad \text{on } \Gamma_c^- \tag{18}$$

in which $\mathbf{n}_\Gamma$ represents the outwards facing normal of their respective boundaries, and $\overline{\boldsymbol{u}}$ and $\overline{\theta}$ are prescribed displacements and temperatures. Dirichlet boundary conditions are applied to all exterior faces of the rock mass, such that the Neumann boundaries $\Gamma_t = \Gamma_q = \emptyset$. In the modelled system, the temperature is prescribed such that edges of the rock mass domain remain fixed at the initial temperature, $\overline{\theta} = \theta_0$. (15) and (16) represent the tractions on the internal crack surface, Γ_c. (17) and (18) represent the convective heat transfer occurring between the solid and fluid temperature fields on the crack surface and are the counterpart to the body source terms within the conservation of energy in the fluid (12).

The boundary conditions on the fluid domain are

$$p = \overline{p} \quad \text{on } \Gamma_p \tag{19}$$

$$-k\rho_f \nabla p \cdot \mathbf{n}_{\Gamma_Q} = \overline{Q} \quad \text{on } \Gamma_Q \tag{20}$$

$$T = \overline{T} \quad \text{on } \Gamma_T \tag{21}$$

$$-k_f \nabla T \cdot \mathbf{n}_{\Gamma_{q_f}} = \overline{q}_f \quad \text{on } \Gamma_{q_f} \tag{22}$$

in which $\overline{p}$, $\overline{Q}$, and $\overline{T}$ are prescribed pressure, fluid mass flux, and fluid temperature. Pressure is prescribed at the outlet, and is assumed to be constant atmospheric pressure. The boundary Γ_Q exists at (1) the inlet, where the injection rate $\overline{Q}$ is prescribed, and (2) around the edges of the crack domain, such that there is no far-field fluid

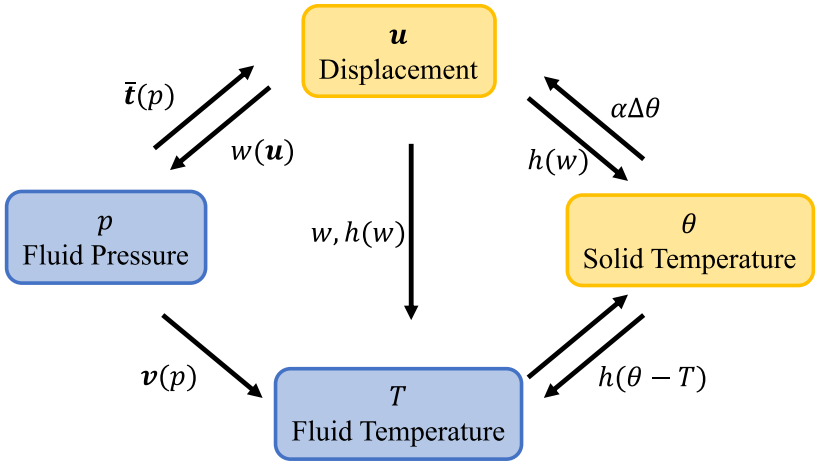

Fig. 4. Representation of the interconnectivity between fields and the methods through which they are coupled.

leakoff. The boundary Γ_T is prescribed at the inlet, such that the temperature of the injected fluid is prescribed. The term $\overline{q}_f$ prescribes the conductive heat flux of the fluid on the boundary Γ_{q_f}, but it does not prevent energy from leaving the domain through an advective heat flux. On the edges of the crack domain, there is no leakoff and the conductive heat flux is prescribed such that $\overline{q}_f = 0$. Unlike the edges of the domain, there exists an advective flux at the outlet. It is assumed that the well pipes are insulated such that the fluid temperature at the end of the pipe is equal to the temperature at the start of the pipe.

The weak forms of the governing equations are derived using the standard method of multiplying the strong forms of the governing equations by weight functions $\delta\boldsymbol{u}, \delta\theta, \delta p, \delta T$, integrating over the respective domains and applying the divergence theorem. The corresponding weak forms of the governing equations are

$$0 = \int_\Omega \nabla\delta\boldsymbol{u} : \boldsymbol{\sigma}\, d\Omega - \oint_{\Gamma_c^+} \delta\boldsymbol{u} \cdot (p\mathbf{I} - \boldsymbol{\sigma}_0 + \bar{t}_{con}\mathbf{I}) \cdot \mathbf{n}_{\Gamma_c^+} d\Gamma \tag{23}$$
$$- \oint_{\Gamma_c^-} \delta\boldsymbol{u} \cdot (p\mathbf{I} - \boldsymbol{\sigma}_0 + \bar{t}_{con}\mathbf{I}) \cdot \mathbf{n}_{\Gamma_c^-} d\Gamma$$

$$\int_\Omega \delta\theta \rho_s c_{ps} \dot{\theta}\, d\Omega = \int_\Omega \nabla\delta\theta \cdot k_s \nabla\theta\, d\Omega - \oint_{\Gamma_c^+} \delta\theta h(w)\,(\theta - T) d\Gamma \tag{24}$$
$$- \oint_{\Gamma_c^-} \delta\theta h(w)\,(\theta - T) d\Gamma$$

$$0 = \oint_{\Gamma_c} \nabla\delta p \cdot\ k \nabla p\, d\Gamma - \oint_{\Gamma_c} \nabla\delta p \cdot\ k\rho_f \boldsymbol{g}\, d\Gamma_c + \delta p|_{\Gamma_Q} \overline{Q} \tag{25}$$

$$0 = \oint_{\Gamma_c} \nabla\delta T \cdot w k_f \nabla T\, d\Gamma + \oint_{\Gamma_c} \delta T \rho_f c_{pf} w\boldsymbol{v} \cdot \nabla T\, d\Gamma \tag{26}$$
$$- \oint_{\Gamma_c} \delta T h(w)(\langle\!|\theta|\!\rangle - 2T) d\Gamma$$

in which $\langle\!|\theta|\!\rangle = (\theta|_{\Gamma_c^+} + \theta|_{\Gamma_c^-})$ denotes the sum of the temperature along both crack faces. The corresponding coupled problem is then to find the fields $\boldsymbol{u}, \theta, p, T$ such that the weak forms of the governing equations are satisfied. The coupling between the fields is illustrated in Fig. 4, which shows that there is a high degree of interconnectivity and dependence between the fields.

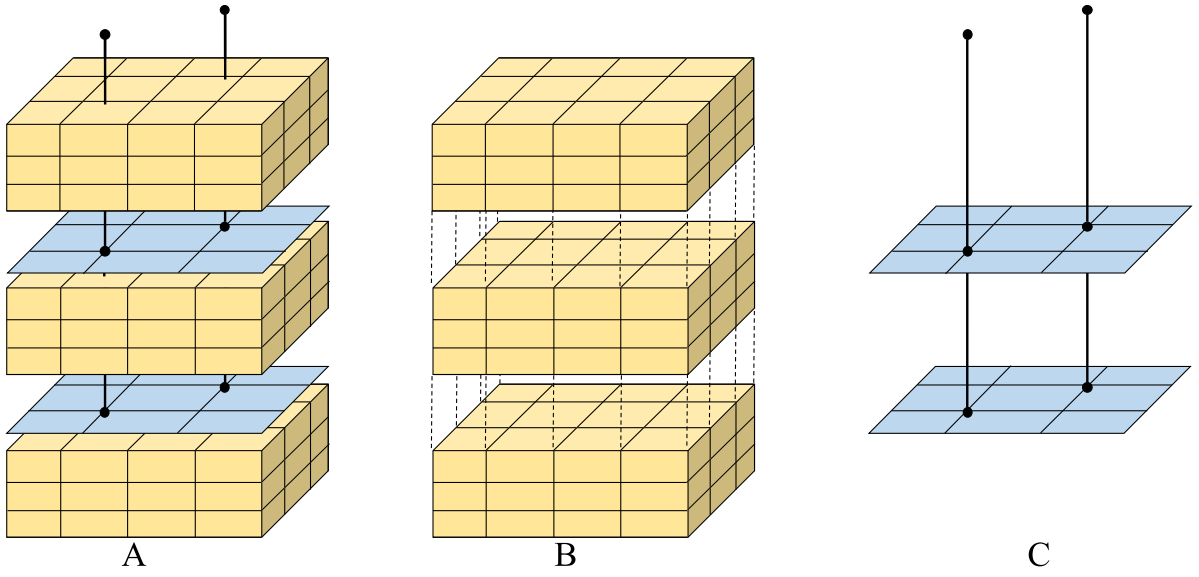

Fig. 5. Assembly of the EGS well model using three dimensional rock masses, two dimensional fracture planes, and one dimensional well pipes. Image A shows the complete assembly of the model. Image B shows the solid domain blocks, which are connected to each other through shared nodes around the edges of the fracture planes. Image C shows the fluid domain which comprises of two dimensional fracture planes and one dimensional well pipes. The fracture planes are connected to each other and the surface through the well pipes. The well pipes pass through the rock mass blocks, but do not interact with them.

2.2. Discretization

This section describes the discretization of the problem into semi-discrete equations using the finite element method, and discrete equations using the β-method of time integration. Fig. 5 shows the assembly of the model using three dimensional blocks of rock mass, two dimensional fracture planes, and one dimensional well pipes.

2.2.1. Semi-discrete equations

The solid domain is discretized into three-dimensional elements. The two solid fields, $\boldsymbol{u}$ and θ, are discretized such that at point $\mathbf{X} \in \Omega$ and time t, the approximations are approximated as

$$\boldsymbol{u}^h(\mathbf{X}, t) = \sum_I N_I(\mathbf{X})\boldsymbol{u}_I(t) \equiv \mathbf{N}(\mathbf{X})\mathbf{u}(t) \tag{27}$$

$$\theta^h(\mathbf{X}, t) = \sum_I N_I(\mathbf{X})\theta_I(t) \equiv \mathbf{N}(\mathbf{X})\boldsymbol{\theta}(t) \tag{28}$$

in which I is the set of nodes in the solid mesh. $N_I(\mathbf{X})$ denotes the standard finite element shape functions for eight node brick elements, while $\boldsymbol{u}_I(t)$ and $\theta_I(t)$ denote the displacement and temperature degrees of freedom at each solid element node in the mesh. $\mathbf{N}(\mathbf{X})$, $\mathbf{u}(t)$, and $\boldsymbol{\theta}(t)$ are the matrix form representations of the shape function and degree of freedom vectors.

The fluid temperature and pressure fields in the fracture planes are discretized into two-dimensional elements such that the nodes and elements of the fracture surface coincide with those of the adjacent solid mesh. The well pipes are discretized using one dimensional elements. A finite element approximation is used for the fluid fields. In this implementation, four node quadrilateral Q4 elements are used for the elements in the crack plane, while two node linear L2 elements are used for the well pipes. Conservation of mass within well pipes with uniform properties dictates that the pressure gradient must be constant along the length of the pipe, so a single L2 element is sufficient to connect fracture planes to each other or to the surface and reproduce the exact pressure distribution in the pipes.

The approximated fluid fields, p^h and T^h at point $\mathbf{X} \in \Gamma_c$ and time t are approximated by

$$p^h(s,t) = \sum_M \psi_M(\mathbf{X}) p_M(t) \equiv \boldsymbol{\psi}(\mathbf{X})\mathbf{p}(t) \tag{29}$$

$$T^h(s,t) = \sum_M \psi_M(\mathbf{X}) T_M(t) \equiv \boldsymbol{\psi}(\mathbf{X})\mathbf{T}(t) \tag{30}$$

in which M is the set of all nodes in the fluid mesh. $\boldsymbol{\psi}(\mathbf{X})$ is the matrix of two dimensional shape functions while $\mathbf{p}(t)$ and $\mathbf{T}(t)$ denote the vectors of nodal degrees of freedom for the pressure and fluid temperature fields, respectively.

Substituting these approximations into the weak forms of the governing equations, the semi-discrete form of the coupled system is

$$\begin{bmatrix} \mathbf{R}_u(\mathbf{u},\mathbf{p},\boldsymbol{\theta}) \\ \mathbf{R}_p(\mathbf{u},\mathbf{p}) \\ \mathbf{R}_\theta(\mathbf{u},\boldsymbol{\theta},\mathbf{T}) \\ \mathbf{R}_T(\mathbf{u},\mathbf{p},\boldsymbol{\theta},\mathbf{T}) \end{bmatrix} = \begin{bmatrix} \mathbf{F}_{uu} - \mathbf{F}_{up} - \mathbf{F}_{\Gamma_t} \\ \mathbf{F}_p - \mathbf{F}_{\Gamma_Q} - \mathbf{F}_g \\ \mathbf{C}\dot{\boldsymbol{\theta}} - \mathbf{F}_{\theta\theta} - \mathbf{F}_{\theta T} - \mathbf{F}_{\Gamma_q} \\ -\mathbf{F}_{T\theta} + \mathbf{F}_{TT} \end{bmatrix} = \mathbf{0} \tag{31}$$

The definitions of the vectors in the residuals are given in Appendix.

2.2.2. Discrete equations

The rate of temperature change within the solid is often discretized using the β-method, such that

$$\dot{\boldsymbol{\theta}} = \frac{\boldsymbol{\theta}^n - \boldsymbol{\theta}^{n-1}}{\Delta t} \tag{32}$$

$$\Delta t = t^n - t^{n-1} \tag{33}$$

$$\mathbf{C}\frac{\boldsymbol{\theta}^n - \boldsymbol{\theta}^{n-1}}{\Delta t} = (1-\beta)F(t^n) + \beta F(t^{(n-1)}) \tag{34}$$

in which $\boldsymbol{\theta}^n$ is the vector of solid temperatures at time n. The β-method is susceptible to the development of spurious oscillations [34,35] under the following conditions: (a) the thermal boundary layers are small relative to the scale of the problem, (b) the thermal diffusivity is low relative to the scale of the problem, and (c) the timesteps are small relative to the scale of the problem. In our experience, these conditions occur when modelling EGS and using typical ranges for dimensions, timesteps, and diffusivities. We implemented the β method using a Crank–Nicolson method ($\beta = 0.5$) and observed the development of these spurious oscillations in the solution. $\beta = 0$ yields a Backwards Euler method of time integration, and while it only provides $O(t)$ accuracy, it provides higher numerical damping and mitigates the development of spurious oscillations compared to other values of β [35]. Therefore, β is set to 0 and the complete set of coupled discrete equations is

$$\begin{bmatrix} \mathbf{R}_u(\mathbf{u},\mathbf{p},\boldsymbol{\theta}) \\ \mathbf{R}_p(\mathbf{u},\mathbf{p}) \\ \mathbf{R}_\theta(\mathbf{u},\boldsymbol{\theta},\mathbf{T}) \\ \mathbf{R}_T(\mathbf{u},\mathbf{p},\boldsymbol{\theta},\mathbf{T}) \end{bmatrix}^n = \begin{bmatrix} \mathbf{F}^n_{uu} - \mathbf{F}^n_{up} - \mathbf{F}^n_{\Gamma_t} \\ \mathbf{F}^n_p - \mathbf{F}^n_{\Gamma_Q} - \mathbf{F}^n_g \\ \frac{\mathbf{C}}{\Delta t}(\boldsymbol{\theta}^n - \boldsymbol{\theta}^{n-1}) - (\mathbf{F}^n_{\theta\theta} + \mathbf{F}^n_{\theta T} + \mathbf{F}^n_{\Gamma_q}) \\ -\mathbf{F}^n_{T\theta} + \mathbf{F}^n_{TT} \end{bmatrix} = 0 \tag{35}$$

Recent developments by van Duijn et al. [36] have shown that for the semi-discrete incremental form of the equations governing thermoporoelasticity, the free energy of the system acts as a Lyapunov functional and provides global stability to the time stepping process. It is not clear whether the equations which govern an EGS, which are simplified in the rock mass but expanded in the fractures, admit the same properties. While such an analysis is desirable in the future, it is beyond the scope of this article.

2.2.3. Advection stabilization

Simulation of advection dominated flows, as found in this system, using standard Galerkin finite elements produces solutions with spurious oscillations. To overcome this problem, stabilization is added to the fluid

temperature using a Streamline-Upwind-Petrov–Galerkin (SUPG) method [37]. The modified fluid temperature residual with SUPG stabilization becomes

$$\mathbf{R}_T^n = -\mathbf{F}_{T\theta} + \mathbf{F}_{TT} + \mathbf{F}_{stab} \tag{36}$$

$$\mathbf{F}_{stab} = \oint_{\Gamma_c} \mathbb{B}^\top \cdot \boldsymbol{v} w \rho_f c_{pf} \cdot \tau \cdot \Re(T^h) d\Gamma \tag{37}$$

in which $\Re(T^h)$ is the residual of the strong form of the governing equation (12) into which the approximation, T^h is substituted. τ is the stabilization parameter defined as

$$\tau = \frac{l^e}{2w\|\boldsymbol{v}\|\rho_f c_{pf}}(1 + \frac{9}{Pe^2} + (\frac{l^e}{2w\|\boldsymbol{v}\|\rho_f c_{pf}}h)^2)^{-0.5} \tag{38}$$

in which Pe is the Peclet number, defined as $Pe = \|\boldsymbol{v}\|\rho_f c_{pf}/k_f$, and l^e [m] is the element length [38]. For a two-dimensional element, l^e is defined as the square root of the element area. The exact form of $\Re(T^h)$ depends on the order of the shape functions ψ. For linear elements, the second derivative of the approximation is zero, so the residual is

$$\Re(T^h) = w\rho_f c_{pf} \boldsymbol{v} \cdot \nabla T^h - h(\langle\!\langle \theta \rangle\!\rangle - 2T^h) \tag{39}$$

3. Solution methodologies

This section details five different methodologies for solving the coupled set of discrete non-linear equations given by (35) and modified by (36):

1. a fully-coupled algorithm in which all fields are solved simultaneously (FC)
2. a fully-coupled algorithm in which all fields are solved simultaneously, but Aitken relaxation is used to improve the rate of convergence (FCA)
3. two sequentially-coupled algorithms in which
   (a) temperature fields are solved simultaneously, then displacement and fluid pressure are solved individually (S-Tθ-U-P)
   (b) temperature fields are solved simultaneously, then displacement and fluid pressure are solved simultaneously (S-Tθ-UP)
4. a loosely-coupled one-pass algorithm in which temperature fields are solved simultaneously, then displacement and fluid pressure are solved simultaneously (LC)

3.1. Fully Coupled (FC)

The Newton–Raphson iterative method is used to linearize the set of nonlinear discrete equations and create a fully coupled Jacobian matrix that solves for all four fields simultaneously. The Jacobian of the coupled system at iteration i and time t^n is defined as

$$\mathbf{J}_i^n = \begin{bmatrix} \frac{\partial \mathbf{R}_u}{\partial \mathbf{u}} & \frac{\partial \mathbf{R}_u}{\partial \mathbf{p}} & \frac{\partial \mathbf{R}_u}{\partial \boldsymbol{\theta}} & \frac{\partial \mathbf{R}_u}{\partial \mathbf{T}} \\ \frac{\partial \mathbf{R}_p}{\partial \mathbf{u}} & \frac{\partial \mathbf{R}_p}{\partial \mathbf{p}} & \frac{\partial \mathbf{R}_p}{\partial \boldsymbol{\theta}} & \frac{\partial \mathbf{R}_p}{\partial \mathbf{T}} \\ \frac{\partial \mathbf{R}_\theta}{\partial \mathbf{u}} & \frac{\partial \mathbf{R}_\theta}{\partial \mathbf{p}} & \frac{\partial \mathbf{R}_\theta}{\partial \boldsymbol{\theta}} & \frac{\partial \mathbf{R}_\theta}{\partial \mathbf{T}} \\ \frac{\partial \mathbf{R}_T}{\partial \mathbf{u}} & \frac{\partial \mathbf{R}_T}{\partial \mathbf{p}} & \frac{\partial \mathbf{R}_T}{\partial \boldsymbol{\theta}} & \frac{\partial \mathbf{R}_T}{\partial \mathbf{T}} \end{bmatrix}_i^n = \begin{bmatrix} \mathbf{K}_{uu} & \mathbf{K}_{up} & \mathbf{K}_{u\theta} & \mathbf{0} \\ \mathbf{K}_{pu} & \mathbf{K}_{pp} & \mathbf{0} & \mathbf{0} \\ \mathbf{K}_{\theta u} & \mathbf{0} & \mathbf{K}_{\theta\theta} & \mathbf{K}_{\theta T} \\ \mathbf{K}_{Tu} & \mathbf{K}_{Tp} & \mathbf{K}_{T\theta} & \mathbf{K}_{TT} \end{bmatrix}_i^n \tag{40}$$

The entries of the system Jacobian are defined in Appendix. The increments in the primary variables at the ith iteration and time t^n satisfies

$$\mathbf{J}_i^n \Delta \mathbf{d}_i^n + \mathbf{R}_i^n = \mathbf{J}_i^n \begin{bmatrix} \Delta\mathbf{u} \\ \Delta\mathbf{p} \\ \Delta\boldsymbol{\theta} \\ \Delta\mathbf{T} \end{bmatrix}_i^n + \begin{bmatrix} \mathbf{R}_u \\ \mathbf{R}_p \\ \mathbf{R}_\theta \\ \mathbf{R}_T \end{bmatrix}_i^n = \mathbf{0} \tag{41}$$

therefore,

$$\Delta \mathbf{d}_i^n = -(\mathbf{J}_i^n)^{-1}\mathbf{R}_i^n \tag{42}$$

and the primary variables can be updated as

$$\mathbf{d}_{i+1}^n = \mathbf{d}_i^n + \Delta \mathbf{d}_i^n \tag{43}$$

The fully coupled algorithm is illustrated in Fig. 6. Convergence is defined using a modified L2-norm of the system residual in which the norm of each field has been non-dimensionalized by a meaningful scalar quantity. A normalized residual allows the relative error to be compared between all four fields, each of which have different units and may differ by orders of magnitude. The modified dimensionless norm, $\|\mathbf{R}^*\|$, is defined as

$$\|\mathbf{R}^*\| = \left(\left(\frac{\|\mathbf{R}_u\|}{n_s u^*} \right)^2 + \left(\frac{\|\mathbf{R}_p\|}{n_f p^*} \right)^2 + \left(\frac{\|\mathbf{R}_\theta\|}{n_s \theta^*} \right)^2 + \left(\frac{\|\mathbf{R}_T\|}{n_f T^*} \right)^2 \right)^{0.5} \tag{44}$$

$$u^* = \oint_{\Gamma_c^+} \boldsymbol{\sigma}_0 \cdot \mathbf{n}_{\Gamma_c^+} d\Gamma \tag{45}$$

$$p^* = \overline{Q} \tag{46}$$

$$\theta^* = \overline{Q} c_{pf} (\theta_0 - \overline{T}) \tag{47}$$

$$T^* = \overline{Q} c_{pf} (\theta_0 - \overline{T}) \tag{48}$$

in which n_s is the number of nodes in the solid mesh and n_f is the number of nodes in the fluid mesh. u^*, p^*, θ^*, T^* [N, kg/s, W, W] are scalar quantities which are used to define the relative error. The choice of scaling parameters is problem specific. These scaling parameters have been selected as they provide an order of magnitude estimate for the magnitude of the forcing vectors within the residual of a given field (e.g $u^* \sim \|\mathbf{F}_{up}\|$). Additionally, these scaling parameters are constant within a given timestep and thus do not change between iterations. In this manner, the relative error in the displacement field is defined such that the total error in the force per node should be small compared to the total force acting on a single crack face due to the in-situ stress, u^*. The relative error in the pressure field is defined such that the total error in the fluid flux per node should be small compared to the total fluid flux entering the system, p^*. The relative error in the temperature fields is defined such that the total error in the temperature fluxes should be small compared to the advective flux entering the system, θ^*, T^*. The system is then defined to be converged when $\|\mathbf{R}^*\| < \tau^*$, in which τ^* is a dimensionless admissible relative error for the system. In order for the total error norm of the system to meet the convergence tolerance, τ^*, the relative error of each individual field must also be less than τ^*.

3.2. Fully Coupled Algorithm with dynamic relaxation (FCA)

For this algorithm, Aitken's Δ^2 relaxation method is used to improve the rate of convergence of the Newton–Raphson method. Aitken's Δ^2 relaxation method uses the residuals from the previous two iterations in order to improve the current solution [39]. It is both computationally inexpensive and easy to implement. Its use has been well established in the realm of fluid–structure interaction problems where it is known to improve the rate of convergence for both monolithic and sequential schemes [40]. The FC algorithm is enhanced by replacing (43) using the following steps:

1. Set

$$\mathbf{d}'_{i+1} = \mathbf{d}_i + \Delta \mathbf{d}_i \tag{49}$$

2. Calculate the relaxation parameter, ω_i

$$\omega_i = -\omega_{i-1} \frac{\Delta \mathbf{d}_{i-1}^\top (\Delta \mathbf{d}_i - \Delta \mathbf{d}_{i-1})}{|\Delta \mathbf{d}_i - \Delta \mathbf{d}_{i-1}|^2} \tag{50}$$

3. Update the current solution guess with the relaxation parameter

$$\mathbf{d}_{i+1} = (1 - \omega_i)\mathbf{d}_i + \omega_i \mathbf{d}'_{i+1} \tag{51}$$

4. Resume the regular Newton–Raphson procedure.

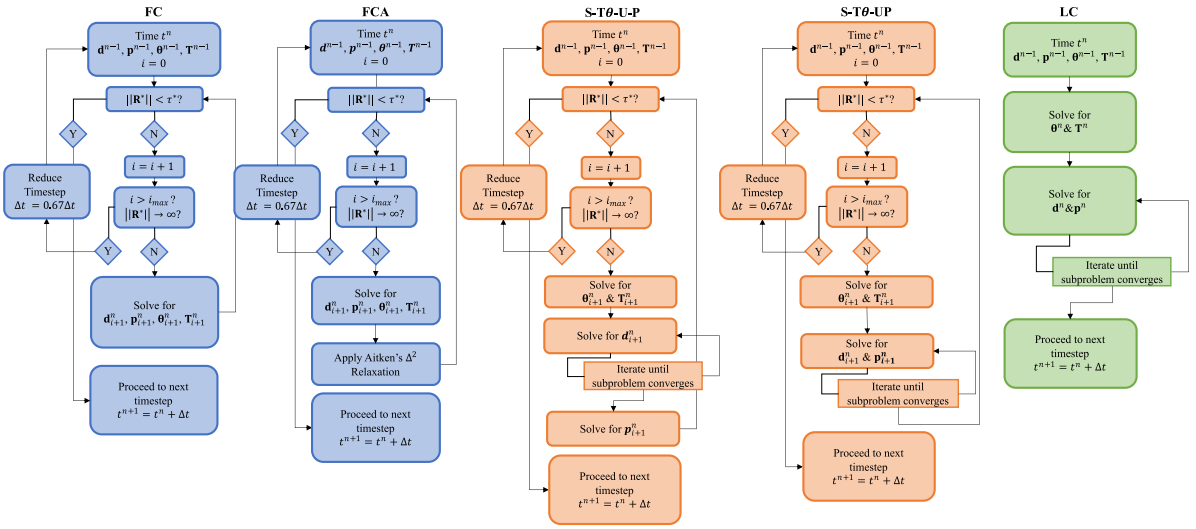

Fig. 6. Flowcharts for the fully, sequentially, and loosely coupled solution algorithms. τ^* represents the admissible relative error on the Newton–Raphson iteration, and i_{max} is the set maximum number of iterations.

The FCA algorithm is illustrated in Fig. 6.

3.3. Sequentially coupled algorithm (S-Tθ-U-P)

Sequentially coupled algorithms are popular in practice due to their ease of implementation. Sequential coupling arises naturally when multiple pre-existing solvers are linked together. Compared to the fully coupled scheme, each iteration in a sequentially coupled scheme is less computationally expensive, but more iterations are typically required to converge to a solution. In a sequentially coupled scheme, each field is solved individually in a given iteration by assuming that all other fields are fixed. The S-Tθ-U-P algorithm divides the four fields into three sub-problems: conservation of energy, conservation of mass, and equilibrium of forces. Thus the two temperature fields are solved together, while the fluid flow and deformation problems are solved individually. Furthermore, the discrete form of the subproblem for the fields T and θ is linear for a given $\mathbf{u}$ and p, so it is advantageous to solve the two temperature fields simultaneously. For the S-Tθ-U-P algorithm, the primary variables are updated as follows:

1. Calculate the temperature residuals $\mathbf{R}^n_{\theta i}(\mathbf{u}^n_{i-1}, \boldsymbol{\theta}^n_{i-1}, \boldsymbol{\theta}^{n-1}, \mathbf{T}^n_{i-1})$ and $\mathbf{R}^n_{Ti}(\mathbf{u}^n_{i-1}, \mathbf{p}^n_{i-1}, \boldsymbol{\theta}^n_{i-1}, \mathbf{T}^n_{i-1})$, as well as the tangent matrices $[\mathbf{K}_{\theta\theta}]^n_i(\mathbf{u}^n_{i-1})$, $[\mathbf{K}_{\theta T}]^n_i(\mathbf{u}^n_{i-1})$, $[\mathbf{K}_{T\theta}]^n_i(\mathbf{u}^n_{i-1})$, $[\mathbf{K}_{TT}]^n_i(\mathbf{u}^n_{i-i}, \mathbf{p}^n_{i-1})$
2. Solve for $\Delta\boldsymbol{\theta}^n_i$ and $\Delta\mathbf{T}^n_i$ as follows and update the primary variables

$$\begin{bmatrix}\Delta\boldsymbol{\theta}\\ \Delta\mathbf{T}\end{bmatrix}^n_i = \left(\begin{bmatrix}\mathbf{K}_{\theta\theta} & \mathbf{K}_{\theta T}\\ \mathbf{K}_{T\theta} & \mathbf{K}_{TT}\end{bmatrix}^n_i\right)^{-1}\begin{bmatrix}\mathbf{R}_\theta\\ \mathbf{R}_T\end{bmatrix}^n_i \tag{52}$$

$$\begin{bmatrix}\boldsymbol{\theta}\\ \mathbf{T}\end{bmatrix}^n_i = \begin{bmatrix}\boldsymbol{\theta}\\ \mathbf{T}\end{bmatrix}^n_{i-1} + \begin{bmatrix}\Delta\boldsymbol{\theta}\\ \Delta\mathbf{T}\end{bmatrix}^n_i \tag{53}$$

3. Update the displacement residual $\mathbf{R}^n_{ui}(\mathbf{u}^n_{i-1}, \boldsymbol{\theta}^n_i, \mathbf{p}^n_{i-1})$ and tangent matrix $[\mathbf{K}_{uu}]^n_i(\mathbf{u}^n_{i-1})$
4. Solve for $\Delta\mathbf{u}^n_i$ as follows and update the primary variables

$$\Delta\mathbf{u}^n_i = \left([\mathbf{K}_{uu}]^n_i\right)^{-1}\mathbf{R}^n_{ui} \tag{54}$$

$$\mathbf{u}^n_i = \mathbf{u}^n_{i-1} + \Delta\mathbf{u}^n_i \tag{55}$$

5. Repeat steps 3 and 4 until convergence in the non-linear subproblem is achieved:

$$\frac{\|\mathbf{R}_u\|}{n_s u^*} < \tau^* \tag{56}$$

6. Update the pressure residual $\mathbf{R}^n_{pi}(\mathbf{u}^n_i, \mathbf{p}^n_{i-1})$, and tangent matrix $\left[\mathbf{K}_{pp}\right]^n_i(\mathbf{u}^n_i)$
7. Solve for $\Delta\mathbf{p}^n_i$ as follows and update the primary variables

$$\Delta\mathbf{p}^n_i = \left(\left[\mathbf{K}_{pp}\right]^n_i\right)^{-1}\mathbf{R}^n_{pi} \tag{57}$$

$$\mathbf{p}^n_i = \mathbf{p}^n_{i-1} + \Delta\mathbf{p}^n_i \tag{58}$$

8. Update $\mathbf{R}^n_i$ and check for global convergence.

The S-Tθ-U-P algorithm is illustrated in Fig. 6, where τ^* represents the admissible error on the iteration. The convergence criteria for the sequential algorithm is identical to the fully-coupled algorithm.

3.4. Sequentially coupled algorithm (S-Tθ-UP)

This sequentially coupled algorithm separates the larger problem into two subproblems: a thermal problem, and a mechanical problem. Like the S-Tθ-U-P algorithm, the two temperature fields are simultaneously solved first. However, this algorithm is designed on the premise that there is strong two-way coupling between the fluid pressure and solid deformation, and that the two should not be decoupled. This premise is informed by the results of hydraulic fracturing simulations, in which solving the displacement and pressure fields separately introduces spurious oscillations into the solutions [27]. For the S-Tθ-UP algorithm, the primary variables are updated as follows:

1. Calculate the temperature residuals $\mathbf{R}^n_{\theta i}(\mathbf{u}^n_{i-1}, \boldsymbol{\theta}^n_{i-1}, \boldsymbol{\theta}^{n-1}, \mathbf{T}^n_{i-1})$ and $\mathbf{R}^n_{Ti}(\mathbf{u}^n_{i-1}, \mathbf{p}^n_{i-1}, \boldsymbol{\theta}^n_{i-1}, \mathbf{T}^n_{i-1})$, as well as the tangent matrices $[\mathbf{K}_{\theta\theta}]^n_i(\mathbf{u}^n_{i-1})$, $[\mathbf{K}_{\theta T}]^n_i(\mathbf{u}^n_{i-1})$, $[\mathbf{K}_{T\theta}]^n_i(\mathbf{u}^n_{i-1})$, $[\mathbf{K}_{TT}]^n_i(\mathbf{u}^n_{i-i}, \mathbf{p}^n_{i-1})$
2. Solve for $\Delta\boldsymbol{\theta}^n_i$ and $\Delta\mathbf{T}^n_i$ as follows and update the primary variables

$$\begin{bmatrix}\Delta\boldsymbol{\theta}\\ \Delta\mathbf{T}\end{bmatrix}^n_i = \left(\begin{bmatrix}\mathbf{K}_{\theta\theta} & \mathbf{K}_{\theta T}\\ \mathbf{K}_{T\theta} & \mathbf{K}_{TT}\end{bmatrix}^n_i\right)^{-1}\begin{bmatrix}\mathbf{R}_\theta\\ \mathbf{R}_T\end{bmatrix}^n_i \tag{59}$$

$$\begin{bmatrix}\boldsymbol{\theta}\\ \mathbf{T}\end{bmatrix}^n_i = \begin{bmatrix}\boldsymbol{\theta}\\ \mathbf{T}\end{bmatrix}^n_{i-1} + \begin{bmatrix}\Delta\boldsymbol{\theta}\\ \Delta\mathbf{T}\end{bmatrix}^n_i \tag{60}$$

3. Update the displacement and pressure residuals $\mathbf{R}^n_{ui}(\mathbf{u}^n_{i-1}, \boldsymbol{\theta}^n_i, \mathbf{p}^n_{i-1})$ and $\mathbf{R}^n_{pi}(\mathbf{u}^n_{i-1}, \mathbf{p}^n_{i-1})$, as well as the tangent matrices $[\mathbf{K}_{uu}]^n_i(\boldsymbol{\theta}^n_i)$, $\left[\mathbf{K}_{pu}\right]^n_i(\mathbf{u}^n_{i-1}, \mathbf{p}^n_{i-1})$, $\left[\mathbf{K}_{pp}\right]^n_i(\mathbf{u}^n_{i-i})$
4. Solve for $\Delta\mathbf{u}^n_i$ and $\Delta\mathbf{p}^n_i$ as follows and update the primary variables

$$\begin{bmatrix}\Delta\mathbf{u}\\ \Delta\mathbf{p}\end{bmatrix}^n_i = \left(\begin{bmatrix}\mathbf{K}_{uu} & \mathbf{K}_{up}\\ \mathbf{K}_{pu} & \mathbf{K}_{pp}\end{bmatrix}^n_i\right)^{-1}\begin{bmatrix}\mathbf{R}_u\\ \mathbf{R}_p\end{bmatrix}^n_i \tag{61}$$

$$\begin{bmatrix}\mathbf{u}\\ \mathbf{p}\end{bmatrix}^n_i = \begin{bmatrix}\mathbf{u}\\ \mathbf{p}\end{bmatrix}^n_{i-1} + \begin{bmatrix}\Delta\mathbf{u}\\ \Delta\mathbf{p}\end{bmatrix}^n_i \tag{62}$$

5. Repeat steps 3 and 4 until convergence in the non-linear subproblem is achieved:

$$\left(\left(\frac{\|\mathbf{R}_u\|}{n_s u^*}\right)^2 + \left(\frac{\|\mathbf{R}_p\|}{n_f p^*}\right)^2\right)^{0.5} < \tau^* \tag{63}$$

6. Update $\mathbf{R}^n_i$ and check for global convergence.

The S-Tθ-UP algorithm is illustrated in Fig. 6, where τ^* represents the admissible error on the iteration. The convergence criteria for the sequential algorithm is identical to the fully-coupled algorithm.

3.5. Loosely Coupled (LC)

Loosely coupled algorithms provide another computationally efficient alternative to the fully-coupled scheme. Loosely-coupled schemes are very fast and often give the impression of robustness since they are one-pass schemes and thus do not verify convergence. While it is well known that loosely-coupled schemes are problematic, it is

included in this study since such schemes are often used indiscriminately in practice. For the loosely coupled algorithm, the same solution strategy as the S-Tθ-UP algorithm is adopted, but a one-pass scheme is adopted instead of iterating until convergence. The loosely-coupled algorithm is illustrated in Fig. 6.

4. Verification and convergence study

In this section, the physical model is verified against an existing EGS model and then a simple illustrative problem is constructed to study the convergence properties of the five coupling schemes.

4.1. Verification with existing EGS models

The physical model is verified against an existing EGS model by adopting the example of a single-fracture EGS first presented by Guo et al. [18], and later used as a verification example by Slatlem Vik et al. [24]. The results presented by Guo et al. [18] and Slatlem Vik et al. [24] are not exact solutions, but rather separate numerical models which contain their own set of assumptions. There are several key differences between the models: (1) Guo et al. [18] use a porous media model in which the fracture is modelled as an equivalent thin porous media volume, rather than a two-dimensional manifold; (2) Guo et al. [18] use only a single temperature field to describe the conservation of energy within the combined porous media, rather than two separate fields for rock and fluid temperature (θ and T); (3) Guo et al. [18] use a hyperbolic model to capture the change in fracture aperture as a function of confining stress, rather than the simple additive aperture model adopted here.

A circular fracture with a radius of 1000 m connects an injection and production well at a depth of 3000 m, and an initial fracture aperture of 0.2 mm. The circular fracture, $\Omega_{f\circ}$, is enforced on the two-dimensional square fracture plane through the initial aperture such that $w_0 = 0.2$ mm $\forall \mathrm{X} \in \Omega_{f\circ}$ and $w_0 = 10^{-9}$ mm $\forall \mathrm{X} \notin \Omega_{f\circ}$. The injection and production wells are spaced 500 m apart and cold fluid is injected at a temperature of 50 °C into a 200 °C rock mass at a rate of 12.5 L/s for 30 years. The adopted material properties and boundary conditions are summarized in Table 1. As there is only a single temperature field in the model of Guo et al. [18], the Nusselt number is not present in the model of Guo et al. [18], and is thus treated as a calibration parameter to match the hydro-thermal (TH) production temperature curve from Guo et al. [18]. The Nusselt number, Nu, governs the heat transfer coefficient, h, which controls the rate at which heat is transferred between the solid and the fluid. The heat transfer coefficient is a function of the fracture aperture and is not constant across the fracture plane, $h = h(w^{-1})$. The model is first run while neglecting the mechanical deformations to calibrate the Nusselt number. The model is then run with mechanical deformations (THM), and the results are compared against the works of Guo et al. [18] and Slatlem Vik et al. [24]. The results of this comparison are presented in Fig. 7. The fully-coupled and sequential solution algorithms yield the same results for this problem.

Despite the differences between the models, the results are similar for both the TH and THM cases, with a similar change in the production temperature curves when switching from TH to THM models. Our model predicts 5–10 °C higher production temperatures, but this difference is consistent in both the TH and THM results. This comparison provides confidence to the present physical model and assumptions. In particular, the models of Guo et al. and Slatlem Vik et al. include transient terms in the conservation of mass and conservation of energy of the fluid, which are neglected in the current model. The similar production temperature curves help to validate the assumption of this physical model that these processes may be assumed to be quasi-steady-state.

4.2. Convergence study

Consider a confined reservoir with an array of alternating vertical production and injection wells hydraulically connected by a single infinite horizontal planar fracture. As illustrated in Fig. 8, the injection and production wells are placed at 100 m intervals. The fracture plane is located between 25 m thick reservoir layers. Due to the symmetry of the system, a one-eighth symmetry model is considered. Symmetry boundary conditions are applied on all vertical faces. Normal displacements are constrained on the top and bottom surfaces of the model. The temperature on the bottom face is fixed at the initial temperature, 200 °C, while the top surface is assumed to be insulated. Fluid is injected at a temperature of 70 °C. The thermal boundary conditions were chosen in order to create an asymmetrical temperature field with respect to the fracture plane. The pressure is fixed at 100.15 kPa at the inlet, and 100 kPa at the outlet. The adopted system properties are shown in Table 1.

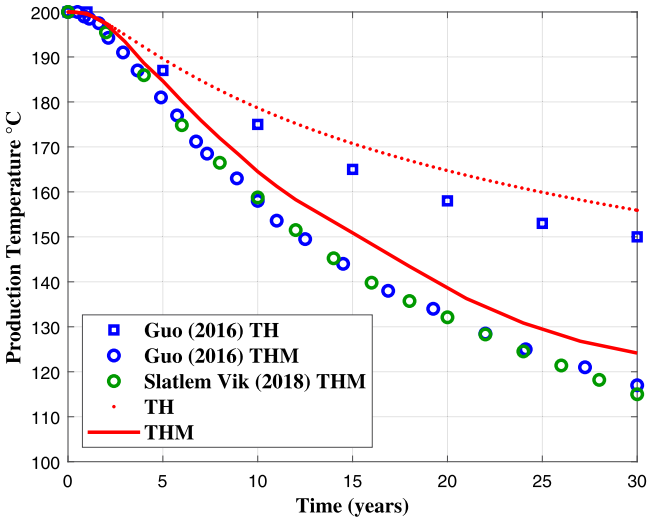

Fig. 7. Verification of physical model against existing EGS models [18,24].

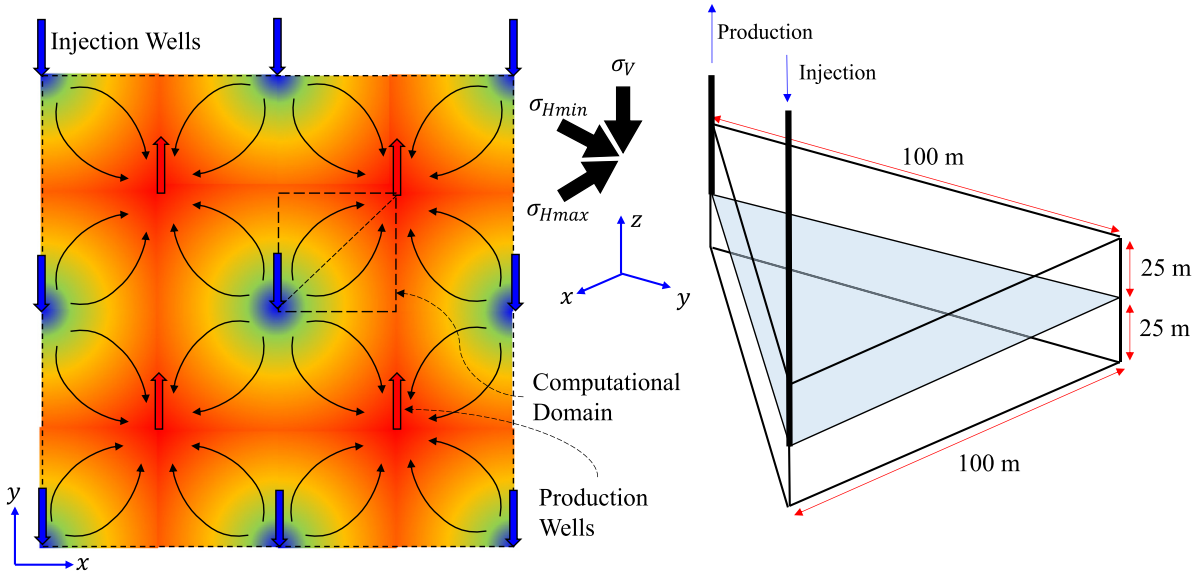

Fig. 8. Problem domain for the convergence study. Injection and production wells are placed at regular intervals on an infinite plane. A one-eighth symmetry model between the injection and production wells is considered.

Injection was simulated for a period of 12 months. The temperature distributions in the rock mass and the fluid in the fracture after 12 months are shown in Fig. 9.

Convergence under mesh refinement was studied using structured meshes with decreasing mesh size and a constant timestep of 1 month. The error was estimated by calculating the difference between the heat flux magnitude, $\|\boldsymbol{q}^h\|$, and an L2-projection of the heat flux magnitude, $\|\boldsymbol{q}_{L2}\|$, which provides an upper bound on the error in the field θ [41]. The relative error estimate with respect to mesh refinement, ϵ_h, was calculated as

$$\epsilon_h = \sqrt{\frac{\int_\Omega \left(\|\boldsymbol{q}^h\| - \|\boldsymbol{q}_{L2}\|\right)^2 d\Omega}{\int_\Omega \|\boldsymbol{q}_{L2}\|^2 d\Omega}} \tag{64}$$

$$\boldsymbol{q}^h = -k_s \nabla \theta^h \tag{65}$$

Table 1
Material parameters and boundary conditions.

Parameters	Variable	Units	Verification study	Convergence study	Sample wells
Rock density	ρ_s	kg/m^3	2500	2600	2600
Elastic modulus	E	GPa	50	50	50
Poisson's ratio	ν	[−]	0.25	0.25	0.25
Rock thermal conductivity	k_s	W/m °C	3.5	6	3
Rock heat capacity	c_{ps}	J/kg °C	790	800	800
Coefficient of thermal expansion	α	$\times 10^{-6}$ m/m °C	8	10	10
Fluid density	ρ_f	kg/m^3	887	1000	1000
Viscosity	μ	mPa s	1.42	1	1
Fluid thermal conductivity	k_s	W/m °C	0.6	0.6	0.6
Fluid heat capacity	c_{pf}	J/kg °C	4460	4200	4200
Nusselt number	Nu	[−]	0.003[a]	5	5
Injection rate	$\overline{Q}$	L/s	12.5	–	25
Injection pressure	$\overline{p}$	kPa	–	100.15	–
Outlet pressure	$\overline{p}$	kPa	100	100	100
Well pipe diameter	D	cm	23	23	23
Depth	L_P	m	3000	350	2000
Initial fracture hydraulic aperture	w_0	mm	0.2	12	4
In-situ stress	σ_V	MPa	64	9	51
	σ_{Hmax}	MPa	100	45	45
	σ_{Hmin}	MPa	70	25	25
Initial reservoir temperature	θ_0	°C	200	200	200
Injection temperature	$\overline{T}$	°C	50	70	70
Distance between wells		m	500	250	250

[a]Fitted parameter.

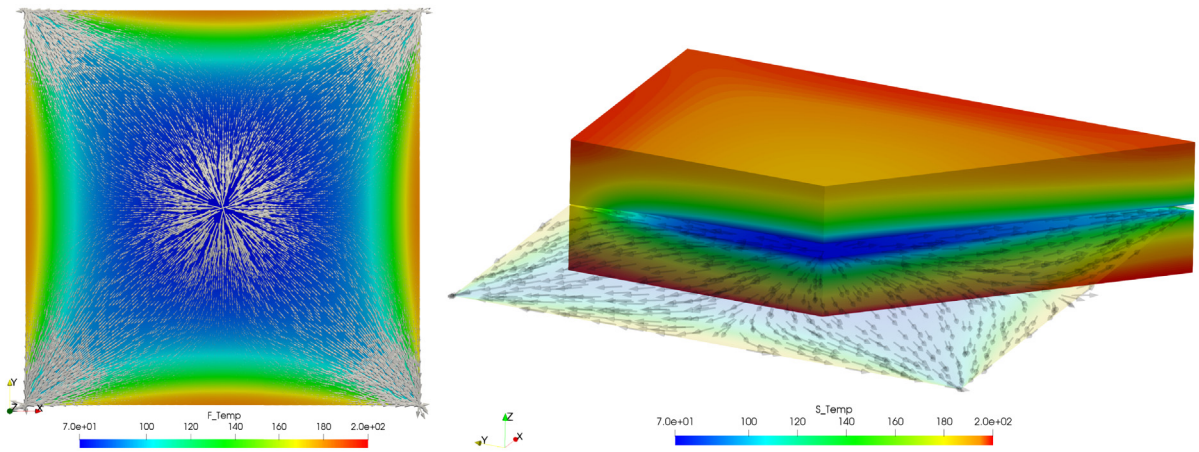

Fig. 9. Temperatures in the fracture plane and rock mass after 12 months for the convergence study problem. The image on the left illustrates the temperature distribution in the fluid, along with scaled velocity vectors indicating the direction of flow within the fracture plane. The image on the right illustrates the temperature distribution in the rock mass (displacements ×150).

Convergence under timestep refinement was studied using a structured mesh with a characteristic mesh size of 3.125 m and with decreasing timestep size. The error estimate for timestep refinement was calculated using the production temperature time history. It was assumed that an exact time history of the production temperature, $T_{ex}(t)$, is given by the FC/FCA algorithms using a timestep of 0.01 months. The accumulative relative error of the production

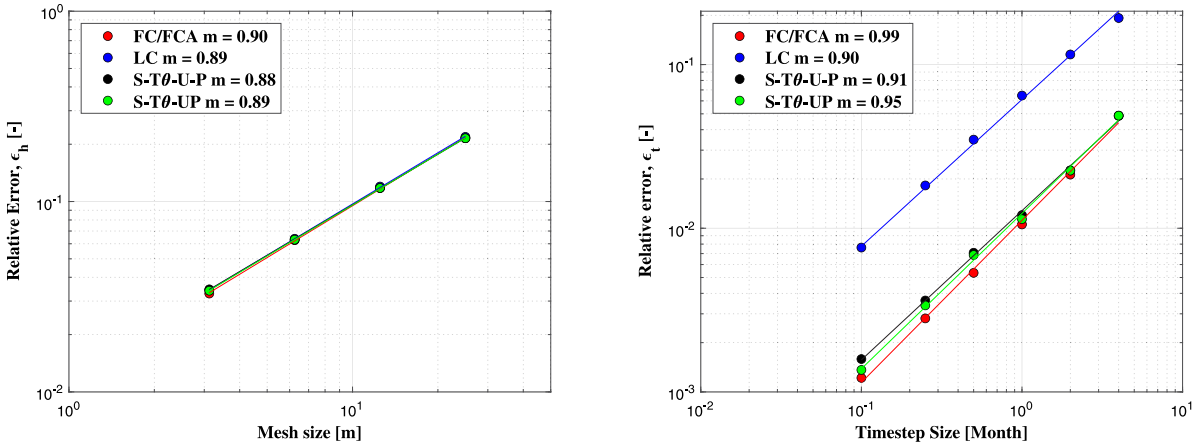

Fig. 10. Convergence of the different solution methodologies with respect to mesh size and timestep refinement. m is the rate of convergence, such that the algorithm displays $O(h^m)$ or $O(\Delta t^m)$ rates of convergence with mesh or timestep refinement.

temperature time history, ϵ_t, was estimated as

$$\epsilon_t = \sqrt{\frac{\int_0^{12}(T^h(t) - T_{ex}(t))^2 dt}{\int_0^{12}(T_{ex}(t))^2 dt}} \tag{66}$$

The convergence of the different solution methodologies is shown in Fig. 10. With respect to mesh refinement, all of the algorithms display similar error and rates of convergence. All of the algorithms display $O(h^{0.9})$ convergence, in which h is a characteristic length of elements in the mesh. The experimental rate of convergence is similar to the $O(h^1)$ convergence of the H1 norm expected in the heat flux field with 8-node brick elements, providing confidence in the results.

With respect to timestep refinement, the FC/FCA algorithm displays a $O(\Delta t^{0.99})$ rate of convergence, which is very close to the ideal $O(\Delta t^1)$ rate of convergence expected from the backwards Euler method of time integration, providing confidence that the algorithm is implemented properly. All of the algorithms display a trend of continuously decreasing error with timestep refinement. The LC algorithm displays the highest relative error and a convergence rate of $O(\Delta t^{0.9})$ for all timesteps, which is near but slightly lower than the expected optimal rate of convergence. The sequential algorithms display errors similar to the FC/FCA algorithms, but slightly suboptimal convergence rates of $O(\Delta t^{0.91})$ and $O(\Delta t^{0.95})$ for the S-Tθ-U-P and S-Tθ-UP algorithms, respectively. The experimental convergence rates provide confidence in the implementation of the fully-coupled and sequential algorithms.

In addition to the timestep and mesh size, the convergence behaviour of algorithms is also affected by the admissible error on the system residual, τ^*, which is used to define convergence of the iterations within a given timestep. Through experimentation, it was found that the FC/FCA were not sensitive to the value of τ^* so long as τ^* was sufficiently small. The sequential algorithms were found to be more sensitive to the value of τ^*, and it was found that τ^* must be reduced as $\Delta t \to 0$. When the timestep was held constant as $\tau^* \to 0$, then the sequential and fully-coupled algorithms converged to the same solution. When τ^* was held constant as $\Delta t \to 0$, it was observed that there exists some timestep size at which the error in the sequential algorithms diverge from the FC/FCA solution towards the LC solution. The FC and LC algorithms thereby act as lower and upper bounds on the error for the sequential algorithms.

5. Comparison of solution methods

This section compares the model results from the different solution strategies for two different EGSs. First the sample problems are described, then the performance of the different solution algorithms is compared in terms of accuracy, robustness, and computational efficiency.

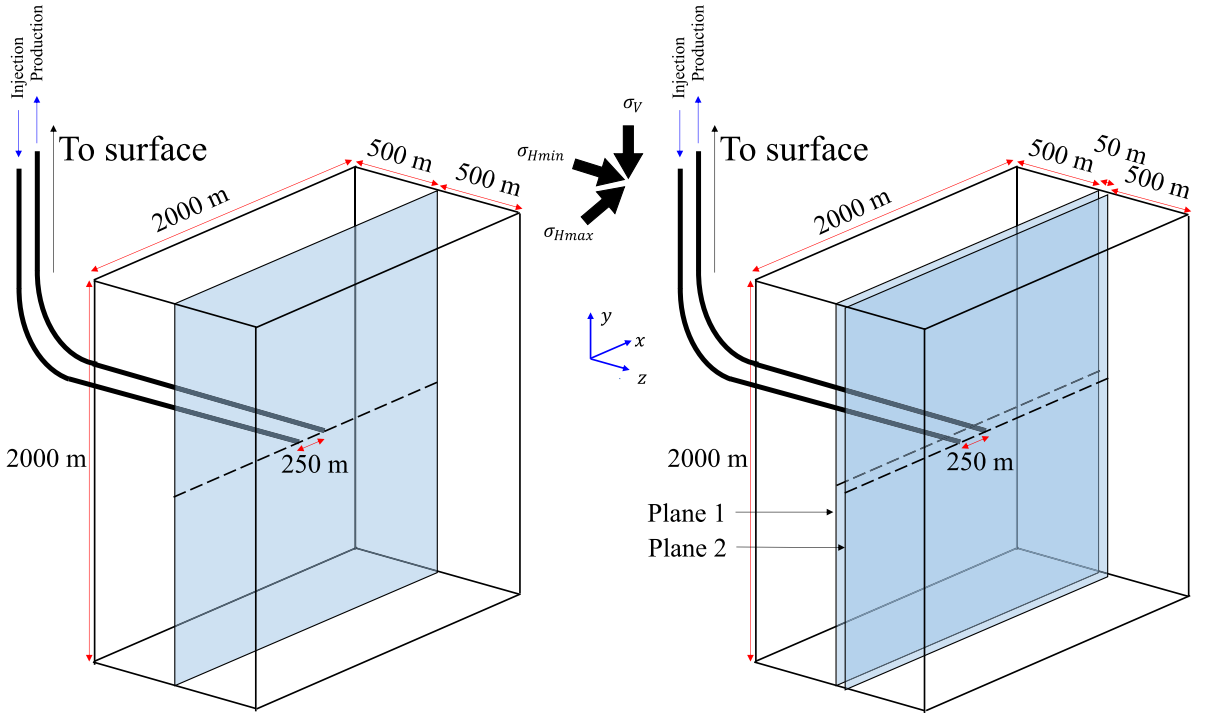

Fig. 11. Computational domains for the sample problems. The image on the left details the domain for the single fracture arrangement while the image on the right details the domain for the double fracture arrangement. The fracture planes are aligned along the XY plane, such that the Y-axis indicates depth.

5.1. Problem description

First, an EGS doublet well is considered where the injection and production wells are hydraulically connected by a single fracture plane. The second case considers an EGS doublet well where the injection and production wells are hydraulically connected by two fracture planes spaced at 50 m. Both EGS wells are illustrated in Fig. 11. Both systems feature vertical crack planes with horizontal injection and production wells spaced 250 m apart at a mean depth of 2000 m. The domain area is 4 km^2 and extends 500 m to either side of the crack planes. The fracture planes extend the entire width and length of the domain. The in-plane effects of gravity on the fluid pressure are neglected, but a hydrostatic pressure head is provided from the depth of wells. On the exterior faces of the solid domain, the temperature is fixed at 200 °C and normal displacements are constrained. The initial temperature is assumed to be uniform throughout the rock mass, and the in-situ stresses are also assumed to be uniform. The material parameters and boundary conditions adopted for these two test cases are shown in Table 1. An initial fracture aperture of 4 mm is adopted. It is assumed that the fractures are propped, so the initial fracture aperture is larger than that of a natural fracture. The impact of the choice of initial aperture is only apparent early on and is primarily reflected in the fluid pressure. Smaller initial apertures lead to much high fluid pressures. Thus, the impact of a larger initial aperture is less than may be expected as it is in part offset by a decrease in mechanical opening due to a decrease in fluid pressure within the fracture. The adopted material parameters assume a granite rock mass and water as a working fluid [1,42–45]. Unlike the single-fracture EGS system studied in Section 4.1, the EGS systems studied here are designed with lower in-situ stresses, higher flow rates, and smaller well spacing in order to ensure that a short-circuiting instability occurs in the life of the system. In this way, the efficiency and robustness of the coupling schemes can be compared under highly nonlinear conditions in which the coupling between physical processes is high.

Both sample problems were simulated for a period of 10 years. The injection rate was applied as a ramping load over the first four months, then kept constant. The single fracture well was solved with timesteps of 1 month throughout the whole simulation, while the two-fracture system was solved with timesteps of 0.75 months for the

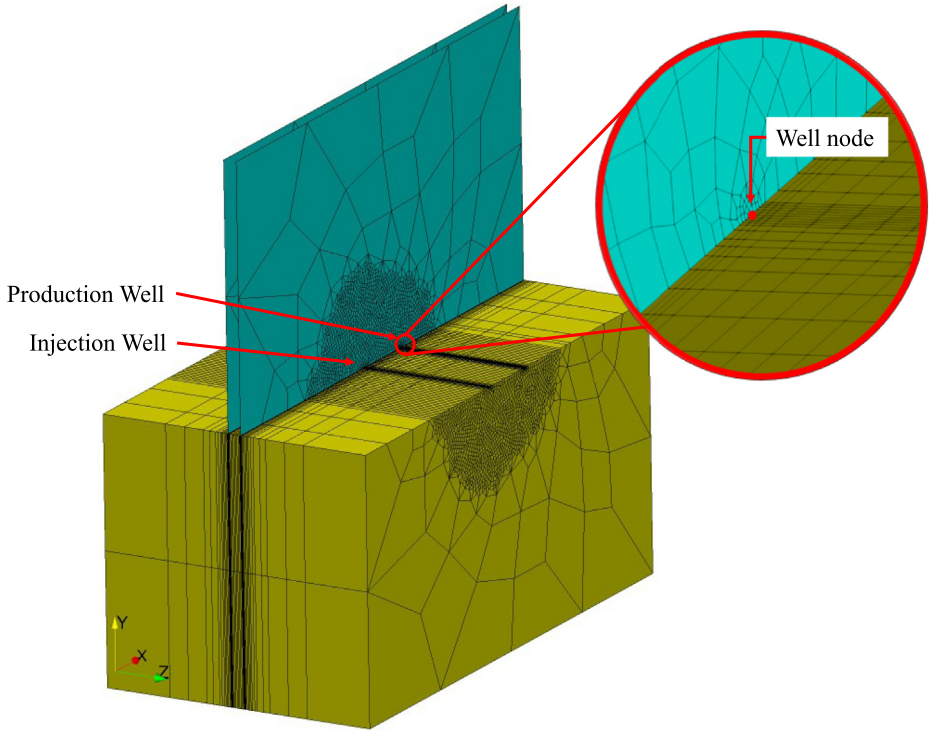

Fig. 12. Illustration of mesh for the two-fracture EGS. A coarse mesh is used around the edge of the domain while a fine mesh is used around the injection and production wells. Symmetry of the system is used along the axis of wells.

first 2 years and 1 month for the following 8 years. If a solution algorithm was unable to converge to a solution with the given timestep, the timestep size was reduced until a converged solution could be found. A solution method was said to be unable to converge to a solution if the number of iterations exceeded a set maximum number of iterations, or the residual was observed to diverge ($\|\mathbf{R}^*\| \to \infty$). The maximum number of iterations was set to 50 for both cases. The maximum iteration number was determined based on our experience with these systems; it was observed that a solution algorithm was generally unlikely to converge if it required more than 50 iterations. A two-dimensional mesh of 1503 nodes and 1447 Q4 elements was taken for a single fracture plane in the approximations of fluid pressure and temperature. The fracture mesh was copied for multiple fractures, and extruded laterally to create the solid mesh, as shown in Fig. 12. The mesh is coarse around the edges of the domain and strategically refined around the well nodes and near the fracture planes. The total number of degrees of freedom were 237,476 for the single fracture problem, and 312,626 for the two fracture problem.

5.2. Results and comparison of solution algorithms

Fig. 13 shows the temperature at the production well and the pressure at the injection well for all five solution algorithms and both EGS systems. There are two temperature breakthroughs observed in Fig. 13a: one at 6 months, and a second at 16 months. Similar behaviour is observed in Fig. 13b, but the two breakthroughs are smeared together and so the transitions are not as distinct. For the first months of operation, the reduction in production temperature is similar to that predicted by a hydro-thermal coupled model and the temperature breakthrough observed at 6 months is likewise a hydro-thermal effect. After approximately 16 months of operations, a second temperature breakthrough is observed and both wells exhibit a rapid decrease in the production temperature due to the opening of a channel within the fracture planes. This second breakthrough is a combined thermo-hydro-mechanical effect and is not observed in a hydro-thermal model. The conductivity of the open channel is very high relative to the rest of the plane, so the flow from the injection well is redirected into the cool channel and away from the hot areas of the plane. The increased flow causes further cooling and aperture growth, encouraging

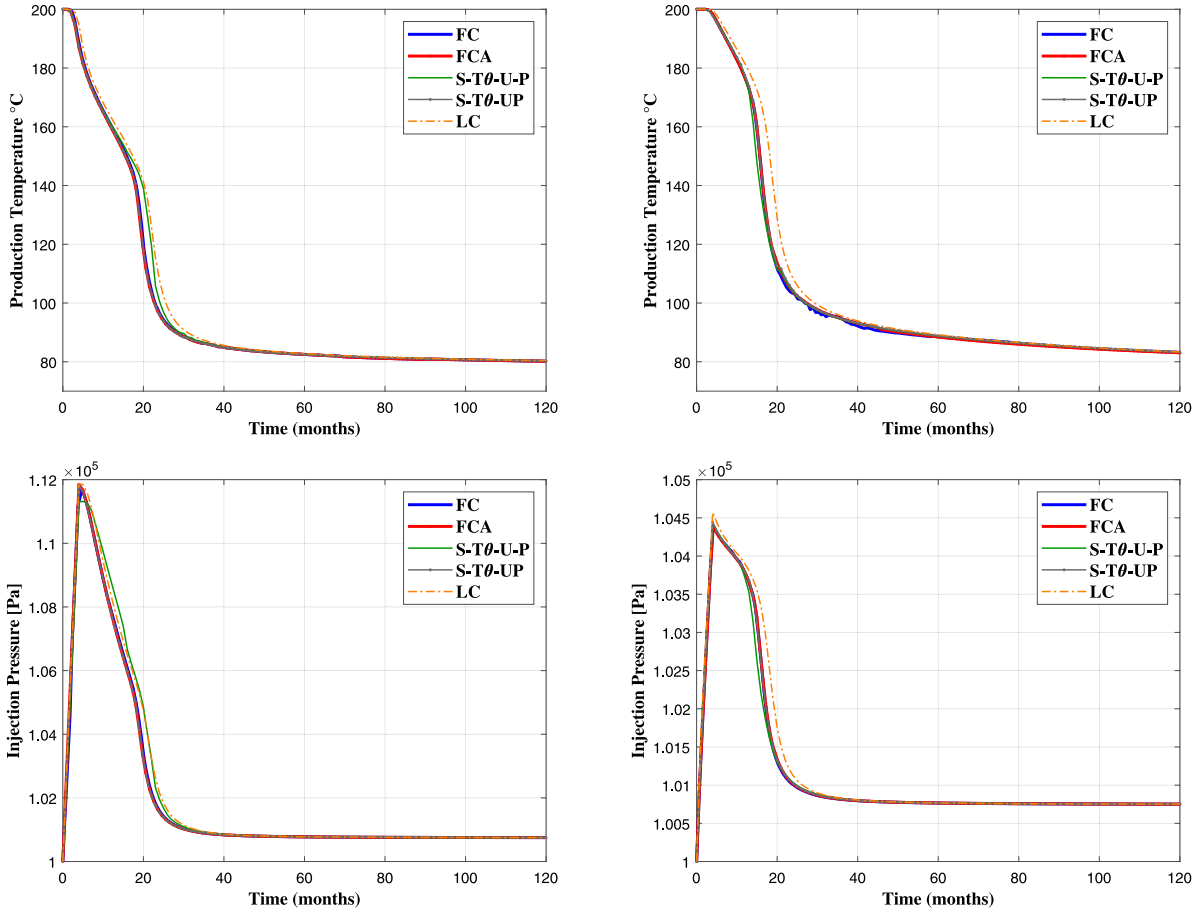

(a) EGS with 1 Fracture Plane

(b) EGS with 2 Fracture Planes

Fig. 13. Inlet and outlet conditions for a single and double crack EGS wells according to different solution algorithms. Production temperature is the temperature of the working fluid from the production well at the surface. Injection pressure is the pressure at the surface to maintain the specified injection flow rate. Pressure within the fracture is higher than the injection pressure due to the hydrostatic pressure head from the well depth.

more fluid to flow through the already cooled and open channel. This process causes the production temperature to decrease very rapidly in a short amount of time in the combined thermo-hydro-mechanical short-circuiting effect known as flow channelling. Fig. 14 shows the temperature distribution in the fluid for the single fracture EGS. The velocity vectors in Fig. 14 show how the fluid changes from a dipole pattern with flow in all directions, to highly restricted flow contained entirely within the channel. Figs. 15 and 16 show the opening of the fracture channel relative to the rest of the fracture plane for the one- and two-fracture EGS respectively. Heat is extracted from both sides of the centre rock mass in the two-fracture EGS, causing increased contraction and larger apertures in the two-fracture EGS. The temperature and pressure distributions in the fracture plane show qualitative agreement with the works of Guo et al. [18] and Slatlem Vik et al. [24].

With respect to the EGS with one fracture plane, the FC, FCA, and S-Tθ-UP algorithms displayed nearly identical results when using the same acceptable relative residual error of $\tau^* = 10^{-5}$. The loosely-coupled solution displays different results from the very start of the simulation, while the S-Tθ-U-P solution begins to deviate after 16 months when the rate of change of the production temperature increases drastically. The impact of the decoupled pressure field in the S-Tθ-U-P algorithm appears in the inlet pressure, where the S-Tθ-U-P algorithm appears to undershoot the peak pressure, then overestimate the inlet pressure until the system reaches a quasi-steady state phase at 40 months. After 40 months, the fracture channel is fully open, and while there are still transient effects occurring

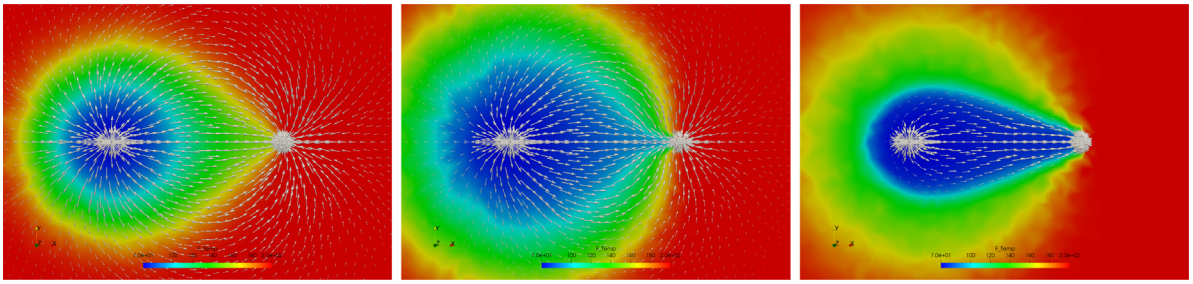

(a) 4 months (b) 18 months (c) 36 months

Fig. 14. Temperature distribution in the fracture fluid over time. Vectors indicating the direction of flow are scaled with the magnitude of fluid velocity. A dipole flow pattern is observed at the beginning of production in which fluid flows in all directions. Channelling develops and redirects the fluid flow as the fracture aperture increases due to heat loss.

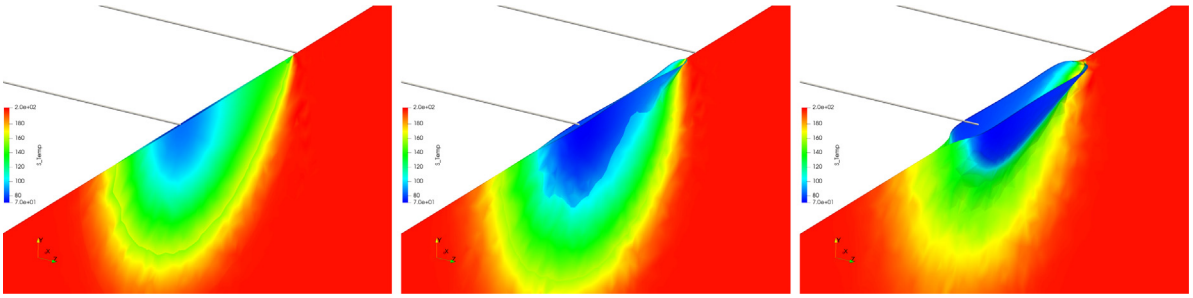

(a) 6 months (b) 18 months (c) 36 months

Fig. 15. Development of an open channel due to heat loss in a single fracture EGS. The temperature in the rock mass is plotted with the displacements and contact penetrations scaled $\times 1500$. The maximum fracture apertures over time are (a) 4.7 mm, (b) 12.7 mm, (c) 30.0 mm. The injection and production wells are shown at their positions in the undeformed configuration. Aperture growth starts symmetrically around the injection well, and on the inlet side of the production well. Over time, the two sections merge to form an open channel in the fracture plane.

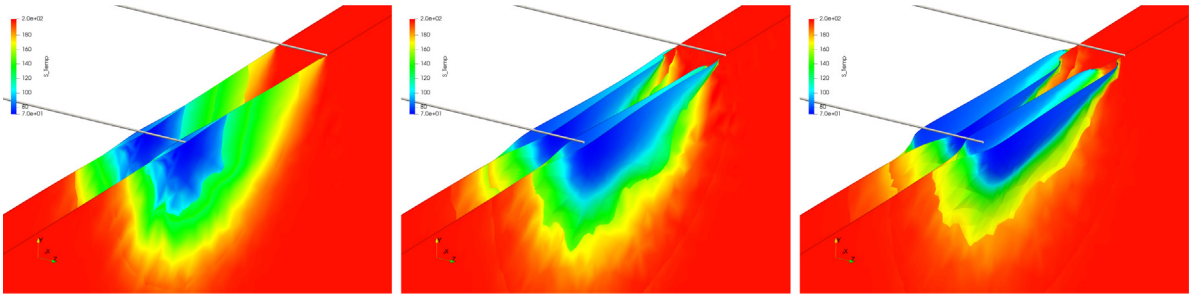

(a) 6 months (b) 18 months (c) 36 months

Fig. 16. Development of an open channel due to heat loss in a two-fracture EGS with 50 m spacing. The temperature in the rock mass is plotted with the displacements and contact penetrations scaled $\times 1000$. The maximum fracture apertures over time in plane 1 are (a) 12.1 mm, (b) 23.8 mm, (c) 38.6 mm. The maximum fracture apertures over time in plane 2 are (a) 12.2 mm, (b) 24.0 mm, (c) 39.0 mm. The injection and production wells are shown at their positions in the undeformed configuration. Aperture growth is larger in the two-fracture EGS because the centre rock mass experiences heat loss from both sides. A clear asymmetry in the deformed shape of the fracture aperture is observed due to the increased contraction of the centre rock mass.

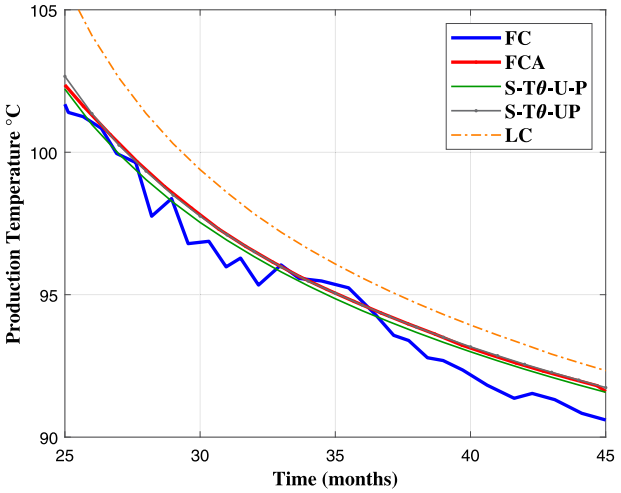

Fig. 17. Production temperature for the double fracture well between 25 and 45 months. Oscillations in the outlet temperature are observed in the FC algorithm and are the results of taking timesteps that are too small for the system.

within the reservoir, there is little further change in the outlet temperature or inlet pressure. There are no spurious oscillations observed in the pressure field with the S-Tθ-U-P algorithm, so it is concluded that the coupled system of equations is not subjected to the same coupling requirements as hydraulic fracture models [27].

With respect to the EGS with two fracture planes, the production temperature from the FC algorithm exhibits oscillations not seen in the other solutions. The FC algorithm suffers from a lack of robustness and needs very small timesteps to converge to a solution. This lack of robustness in the FC algorithm is due to the nature of the coupling between systems. Consider for example the displacement field. It is expected that the aperture will fluctuate between iterations while trying to find a position of equilibrium that satisfies the contact problem. These small changes in the aperture are amplified in the fluid field due to the w^3 term in the Jacobian matrix. These changes in the fluid field can then have huge effects on the fluid temperature distribution, which in turn could then affect the temperature distribution in the solid, which then feeds back into the displacement field. In this manner, small changes in one field can ripple throughout the other fields, making it difficult to find a converged solution. Therefore, the FC algorithm requires small timesteps to converge, especially when the system is changing quickly. Not only does this increase the computation time, but the β-method of time integration becomes susceptible to spurious oscillations if the timestep size is too small [34,35]. This poses a paradoxical problem for the FC algorithm: small timesteps are required to find a converged solution, but small timesteps will also introduce spurious oscillations into the solution. These oscillations are observed in the outlet temperature for the two-fracture EGS between months 25 and 45, even with the Backwards Euler $\beta = 0$. This issue is only observed in the two-fracture EGS as there are additional sources of non-linearity and physical instabilities, such as inter-plane contact and the redistribution of flow between planes, which are not present in the one-fracture EGS. Fig. 17 shows a magnified version of the outlet temperature from the two-fracture system in which the oscillations in the outlet temperature from the FC algorithm are clearly visible. The oscillations only appear in the temperature fields and are present in both fractures in both space and time. The fracture apertures do not experience oscillations, as the magnitude of the oscillations is small and so the rock mass temperature is smooth enough to likewise create a smooth displacement field. These oscillations cannot be reduced by reducing the iteration error tolerance, τ^*. The fully-coupled algorithm therefore produces inaccurate results during periods in which the system experiences strong coupling between the physical processes.

The FCA algorithm does not suffer from the same drawbacks as the FC algorithm. Aitken's Δ^2 relaxation is a simple and cheap addition to the FC algorithm, but it results in immense improvements in the algorithm's performance. Aitken relaxation allows the FCA algorithm to find a converged solution in less than 25 iterations, while the FC algorithm would require more than 50 iterations at the same timestep size, if it converges at all. The improved robustness of the FCA algorithm is demonstrated through Fig. 18, which shows how the addition of relaxation allows the FCA algorithm to continue to converge at a consistent large timestep size while the FC

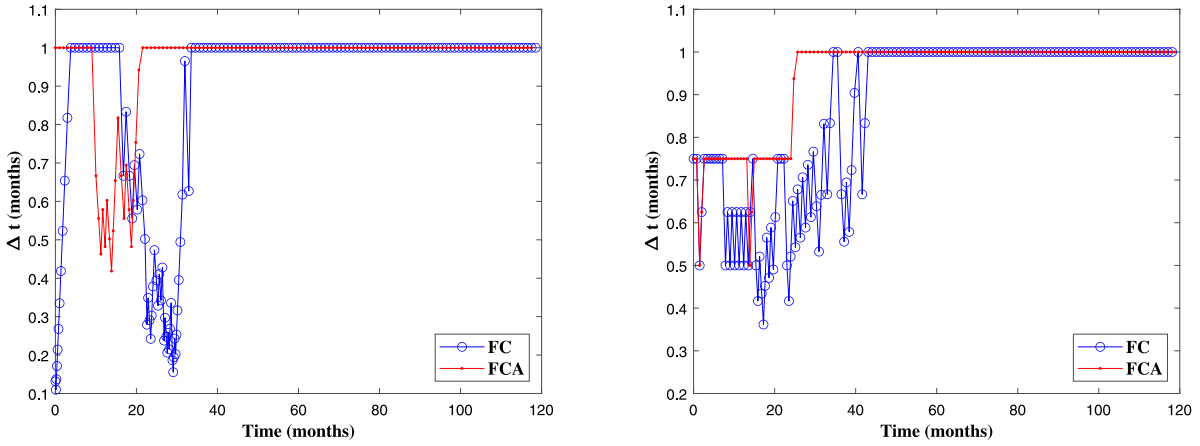

(a) EGS with 1 Fracture Plane

(b) EGS with 2 Fracture Planes

Fig. 18. Timestep sizes for the FC and FCA algorithms throughout the course of the simulations. The timestep size is only decreased if the solution diverged, or hit the set maximum allowable number of iterations (set to 50). Explicit time integration for the same system and mesh would allow a maximum timestep size of 0.05 months.

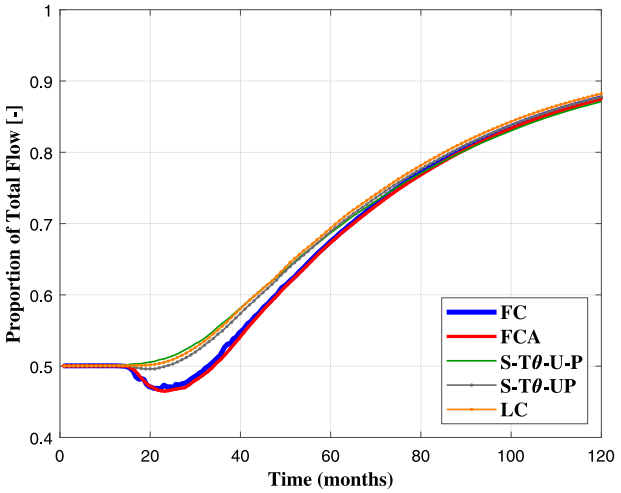

Fig. 19. Proportion of total flow in the dominant crack plane (plane 1) over time for the two fracture EGS. With an admissible error of $\tau^* = 10^{-5}$, only the FC, FCA, and S-Tθ-UP algorithms capture the behaviour in which in the second plane develop channelling before the first plane.

algorithm must frequently reduce its timestep size in order to be able to converge to a solution. This also translates into improved accuracy for the FCA algorithm, as it is less susceptible than the FC algorithm to spurious oscillations. While the addition of Aitken's relaxation improves the robustness of the FCA solution algorithm, further work is needed to determine the requirements for unconditional stability of the time stepping process. The work of van Duijn et al. [36] demonstrates the analysis that is required to show global stability of the system.

With respect to the EGS with two fracture planes, the FCA, S-Tθ-U-P, and S-Tθ-UP solutions all displayed very similar outlet temperatures and inlet pressures when using the same acceptable relative residual error of $\tau^* = 10^{-5}$. However, the proportions of flow over time through each fracture are remarkably different. Fig. 19 illustrates the proportion of total flow in plane 1 and demonstrates how the algorithms yield different behaviour in the reservoir, despite the similar production temperatures and injection pressures. Although the fracture planes are initially identical, an additional pressure head is supplied by the connecting wells, such that the connected fracture-well system is asymmetric and causes plane 2 to open before plane 1. Plane 2 has higher average fluid

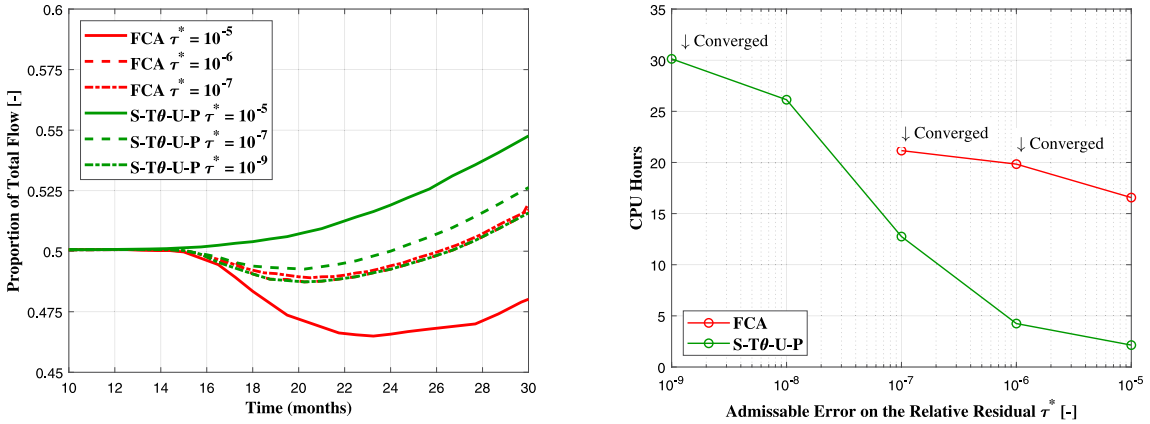

Fig. 20. Reducing tolerance on the FCA and S-Tθ-U-P algorithms and accompanying computation time. The image on the left shows the proportion of flow in the first plane as the admissible iteration tolerance, τ^*, is reduced, demonstrating how the two algorithms converge to the same solution with sufficiently strict tolerances. The image on the right shows the accompanying computation time for the first 30 months of simulation. In order to obtain the converged solution for a given timestep size, the iteration tolerance on the sequential algorithm must be very strict such that it becomes more computationally expensive than the fully-coupled solution.

pressure within the plane such that the average contact stress is slightly lower across plane 2 than it is across plane 1, allowing plane 2 to open before plane 1. Once the channel opens in plane 2, the fluid pressure drops in plane 2, which allows plane 1 to open and develop channelling. Over time, the two fracture EGS system performance decays such that flow is allocated entirely to plane 1. This is a subtle behaviour of the system that is lost in the sequential and loosely-coupled algorithms when using the same convergence criteria as the FCA algorithm.

From the results of the convergence study in Section 4, it is known that the sequential algorithms will converge to the same solution as the fully-coupled algorithms for a given timestep size as the admissible error on the relative residual is reduced, $\tau^* \rightarrow 0$. Using the same admissible relative residual error of $\tau^* = 10^{-5}$, the sequential algorithms appear to offer computational efficiency over the FCA algorithm, with overall computation times for the two fracture EGS of 7 h (S-Tθ-U-P) and 12 h (S-Tθ-UP) compared to 28 h (FCA). As there are discrepancies in the results between the algorithms, this implies that the results are not converged and raises the question: how much must the admissible relative error be reduced to find converged solutions between the different algorithms and what is the accompanying computational cost?

The S-Tθ-U-P and FCA algorithms are considered with increasingly strict tolerance on the admissible iteration error, the results of which are shown in Fig. 20. As the admissible error is reduced, a large change in the results of the FCA algorithm from is observed from $\tau^* = 10^{-5}$ to $\tau^* = 10^{-6}$, but then little change is observed as τ^* is reduced to 10^{-7} indicating that the converged solution for the given timestep scheme has been found. The fully-coupled algorithms have long computation times even at high admissible errors, but decreasing the admissible error is accompanied by a small increase in computational cost, typically only one or two extra iterations. Fig. 20 demonstrates that as the admissible relative error on the residual is refined, the S-Tθ-U-P solution slowly converges towards the FCA results but is accompanied by a large increase in overall computation time. As a result, to obtain a well-converged solution for given timestep scheme, the S-Tθ-U-P algorithm requires such strict tolerances that it loses any computational advantages it appears to offer over the FCA algorithm. Similar behaviour is observed with the S-Tθ-UP algorithm, even though the solution at $\tau^* = 10^{-5}$ is closer to the converged solution than the S-Tθ-U-P algorithm. Thus while the sequential and fully-coupled algorithms produce the same converged solutions with sufficiently small iteration tolerances, in practice the sequential schemes are more computationally expensive if well-converged solutions are sought. It is thus concluded that the advantages of sequential algorithms are relegated to their ease of implementation and reduced memory requirements.

6. Conclusions

In this article, the first comparison of monolithic and sequential solution coupling schemes for thermo-hydro-mechanical modelling of enhanced geothermal systems is presented. A thermo-hydro-mechanical

finite element model is developed for an EGS well consisting of one injection and one production well hydraulically connected by planar fractures. Two monolithic solution schemes are developed — one using the Newton–Raphson iterative method, and one using the Newton–Raphson method modified by Aitken's Δ^2 relaxation method. The monolithic schemes are compared for numerical accuracy and computational efficiency against two sequential schemes and one loosely-coupled scheme.

It is demonstrated fully-coupled solution scheme provides an optimal rate of convergence with mesh and timestep refinement. However, the fully-coupled solution scheme requires very small timesteps in order to converge to a solution, particularly during periods of rapid change within the system, such as the onset of short-circuiting. The requirement for small timesteps introduces spurious oscillations into the solution due to the minimum timestep size of the β-method of time integration. Aitken's Δ^2 relaxation method is shown to increase the robustness of the fully-coupled Newton–Raphson scheme. Aitken relaxation reduces the overall computation time through larger timesteps and fewer iterations, and circumvents the spurious oscillations introduced by the minimum timestep requirement. It is demonstrated that sequential algorithms are capable of producing solutions with the same accuracy and rate of convergence as the monolithic schemes with sufficiently strict iteration tolerances, furthering the verification and providing confidence to the results of previous EGS modelling efforts. No spurious oscillations are observed in the sequential solutions. It is shown that the computation time of the sequential algorithms exceeds that of the monolithic solution schemes when seeking well-converged solutions. Loosely-coupled schemes are shown to provide near optimal rates of convergence with mesh and timestep refinement, but are much less accurate than the monolithic and sequential schemes.

Considerable work remains to be done in exploring the behaviour of enhanced geothermal systems themselves. There are many physical phenomena within these systems that have not been included in this study, such as in-situ stress gradients, temperature gradients, turbulence within the well pipes, heat transfer within the well pipes, and anisotropy within the rock mass. Validation through comparison of modelling results with lab and field experiments is also required to increase confidence in existing modelling efforts.

Declaration of competing interest

The authors declare that they have no known competing financial interests or personal relationships that could have appeared to influence the work reported in this paper.

Acknowledgements

Dr. Gracie acknowledges the support of a Discovery Grant from the Natural Sciences and Engineering Research Council of Canada (NSERC), as well as an Early Researcher Award from the Ontario Ministry of Research and Innovation, Canada. Bruce Gee acknowledges the support of an Alexander Graham Bell Graduate Scholarship from NSERC, Canada, as well as an Engineering Excellence Fellowship from the University of Waterloo, Canada.

Appendix. Definitions of derivative matrices, residual vectors, and Jacobian entries

The solid and fluid fields are discretized using the finite element method. The gradients of the scalar fields, θ^h, p^h, T^h, are defined as

$$\nabla\theta^h(\mathbf{X},t) = \mathbf{B}(\mathbf{X})\boldsymbol{\theta}(t) \tag{A.1}$$

$$\nabla p^h(\mathbf{X},t) = \mathbb{B}(\mathbf{X})\mathbf{p}(t) \tag{A.2}$$

$$\nabla T^h(\mathbf{X},t) = \mathbb{B}(\mathbf{X})\mathbf{T}(t) \tag{A.3}$$

$$\mathbf{B} = \nabla\mathbf{N} \tag{A.4}$$

$$\mathbb{B} = \nabla\boldsymbol{\psi} \tag{A.5}$$

in which $\mathbf{B}$ and $\mathbb{B}$ are the matrices of spatial derivatives of the three and two dimensional shape function vectors

$\mathbf{N}$ and $\boldsymbol{\psi}$, respectively. The stress and strain fields are recast into Voigt form, such that

$$\{\sigma\} = \begin{Bmatrix}\sigma_{11} & \sigma_{22} & \sigma_{33} & \sigma_{23} & \sigma_{13} & \sigma_{12}\end{Bmatrix}^\top \tag{A.6}$$

$$\{\sigma\} - \{\sigma_0\} = \mathbf{D}\left(\{\varepsilon\} - \alpha\Delta\theta\{I\}\right) \tag{A.7}$$

$$\{I\} = \begin{Bmatrix}1 & 1 & 1 & 0 & 0 & 0\end{Bmatrix}^\top \tag{A.8}$$

$$\{\varepsilon\} = \begin{Bmatrix}u_{1,1} & u_{2,2} & u_{3,3} & u_{2,3}+u_{3,2} & u_{1,3}+u_{3,1} & u_{1,2}+u_{2,1}\end{Bmatrix}^\top \tag{A.9}$$

$$\{\varepsilon\} = \{\mathbf{B}\}\mathbf{u} \tag{A.10}$$

in which $\mathbf{D}$ is the matrix form of the elasticity tensor, $\mathbb{C}$, $\{\varepsilon\}$ is the strain tensor, $\boldsymbol{\varepsilon}$, recast into Voigt form, and $\{\mathbf{B}\}$ is the matrix $\mathbf{B}$ rearranged into Voigt form.

The semi-discrete form of the coupled system of equations is given as

$$\begin{bmatrix}\mathbf{R}_u(\mathbf{u},\mathbf{p},\boldsymbol{\theta})\\ \mathbf{R}_p(\mathbf{u},\mathbf{p})\\ \mathbf{R}_\theta(\mathbf{u},\boldsymbol{\theta},\mathbf{T})\\ \mathbf{R}_T(\mathbf{u},\mathbf{p},\boldsymbol{\theta},\mathbf{T})\end{bmatrix} = \begin{bmatrix}\mathbf{F}_{uu}-\mathbf{F}_{up}\\ \mathbf{F}_p-\mathbf{F}_{\Gamma_Q}-\mathbf{F}_g\\ \mathbf{C}\dot{\boldsymbol{\theta}}-\mathbf{F}_{\theta\theta}-\mathbf{F}_{\theta T}\\ -\mathbf{F}_{T\theta}+\mathbf{F}_{TT}+\mathbf{F}_{stab}\end{bmatrix} = 0 \tag{A.11}$$

in which the vectors are defined as

$$\mathbf{F}_{uu} = \int_\Omega \{\mathbf{B}\}^\top\mathbf{D}\{\mathbf{B}\}d\Omega\mathbf{u} - \int_\Omega \{\mathbf{B}\}^\top\mathbf{D}\alpha\begin{bmatrix}\mathbf{N}\\ \mathbf{N}\\ \mathbf{N}\\ 0\\ 0\\ 0\end{bmatrix}d\Omega(\boldsymbol{\theta}-\boldsymbol{\theta}_0) \tag{A.12}$$

$$\mathbf{F}_{up} = \left(\oint_{\Gamma_c^+}\mathbf{N}^\top(p\mathbf{I}+\boldsymbol{\sigma}_0+\bar{t}_{con}\mathbf{I})\mathbf{n}_{\Gamma_c^+}d\Gamma + \oint_{\Gamma_c^-}\mathbf{N}^\top(p\mathbf{I}+\boldsymbol{\sigma}_0+\bar{t}_{con}\mathbf{I})\mathbf{n}_{\Gamma_c^-}d\Gamma\right) \tag{A.13}$$

$$\mathbf{F}_p = \oint_{\Gamma_c}\mathbb{B}^\top\cdot\rho_f w k\nabla p d\Gamma \tag{A.14}$$

$$\mathbf{F}_{\Gamma_Q} = \oint_{\Gamma_Q}\boldsymbol{\psi}^\top\overline{Q}d\Gamma \tag{A.15}$$

$$\mathbf{F}_g = \oint_{\Gamma_c}\mathbb{B}^\top\cdot\rho_f w k\rho_f\boldsymbol{g}d\Gamma \tag{A.16}$$

$$\mathbf{C} = \int_\Omega\mathbf{N}^\top\rho_s c_{ps}\mathbf{N}d\Omega \tag{A.17}$$

$$\mathbf{F}_{\theta\theta} = \int_\Omega\mathbf{B}^\top k_s\mathbf{B}d\Omega\boldsymbol{\theta} \tag{A.18}$$

$$\mathbf{F}_{\theta T} = \oint_{\Gamma_c^+}\mathbf{N}^\top h(w)(\theta|_{\Gamma_c^+}-T)d\Gamma + \oint_{\Gamma_c^-}\mathbf{N}^\top h(w)(\theta|_{\Gamma_c^-}-T)d\Gamma \tag{A.19}$$

$$\mathbf{F}_{T\theta} = \oint_{\Gamma_c^+}\boldsymbol{\psi}^\top h(w)(\theta|_{\Gamma_c^+}-T)d\Gamma + \oint_{\Gamma_c^-}\boldsymbol{\psi}^\top h(w)(\theta|_{\Gamma_c^-}-T)d\Gamma \tag{A.20}$$

$$\mathbf{F}_{TT} = \oint_{\Gamma_c}(\mathbb{B}^\top\cdot w k_f\nabla T + \boldsymbol{\psi}^\top\rho_f c_{pf}w\boldsymbol{v}\cdot\nabla T)d\Gamma \tag{A.21}$$

$$\mathbf{F}_{stab} = \oint_{\Gamma_c}\mathbb{B}^\top\cdot\boldsymbol{v}w\rho_f c_{pf}\cdot\boldsymbol{\tau}\cdot\Re(T^h)d\Gamma \tag{A.22}$$

and the fracture aperture is defined as $w = w_0 + \mathbf{n}_{\Gamma_c}^\top(\mathbf{N}|_{\Gamma_c^+} - \mathbf{N}|_{\Gamma_c^-})\mathbf{u}$.

The Jacobian for the Newton–Raphson method is given as

$$\mathbf{J}_i^n = \begin{bmatrix} \frac{\partial \mathbf{R}_u}{\partial \mathbf{u}} & \frac{\partial \mathbf{R}_u}{\partial \mathbf{p}} & \frac{\partial \mathbf{R}_u}{\partial \boldsymbol{\theta}} & \frac{\partial \mathbf{R}_u}{\partial \mathbf{T}} \\ \frac{\partial \mathbf{R}_p}{\partial \mathbf{u}} & \frac{\partial \mathbf{R}_p}{\partial \mathbf{p}} & \frac{\partial \mathbf{R}_p}{\partial \boldsymbol{\theta}} & \frac{\partial \mathbf{R}_p}{\partial \mathbf{T}} \\ \frac{\partial \mathbf{R}_\theta}{\partial \mathbf{u}} & \frac{\partial \mathbf{R}_\theta}{\partial \mathbf{p}} & \frac{\partial \mathbf{R}_\theta}{\partial \boldsymbol{\theta}} & \frac{\partial \mathbf{R}_\theta}{\partial \mathbf{T}} \\ \frac{\partial \mathbf{R}_T}{\partial \mathbf{u}} & \frac{\partial \mathbf{R}_T}{\partial \mathbf{p}} & \frac{\partial \mathbf{R}_T}{\partial \boldsymbol{\theta}} & \frac{\partial \mathbf{R}_T}{\partial \mathbf{T}} \end{bmatrix}_i^n = \begin{bmatrix} \mathbf{K}_{uu} & \mathbf{K}_{up} & \mathbf{K}_{u\theta} & \mathbf{0} \\ \mathbf{K}_{pu} & \mathbf{K}_{pp} & \mathbf{0} & \mathbf{0} \\ \mathbf{K}_{\theta u} & \mathbf{0} & \mathbf{K}_{\theta\theta} & \mathbf{K}_{\theta T} \\ \mathbf{K}_{Tu} & \mathbf{K}_{Tp} & \mathbf{K}_{T\theta} & \mathbf{K}_{TT} \end{bmatrix}_i^n \tag{A.23}$$

in which the entries of the Jacobian are defined as

$$\mathbf{K}_{uu} = \int_\Omega \{\mathbf{B}\}^\top \mathbf{D}\{\mathbf{B}\} d\Omega + \oint_{\Gamma_c^+} \mathbf{N}^\top \mathbf{n}_{\Gamma_c^+} \frac{\partial \bar{t}_{con}}{\partial w^n} \mathbf{n}_{\Gamma_c^+}^\top \mathbf{N} d\Gamma + \oint_{\Gamma_c^-} \mathbf{N}^\top \mathbf{n}_{\Gamma_c^-} \frac{\partial \bar{t}_{con}}{\partial w^n} \mathbf{n}_{\Gamma_c^-}^\top \mathbf{N} d\Gamma \tag{A.24}$$

$$\mathbf{K}_{up} = \oint_{\Gamma_c^+} \mathbf{N}^\top \mathbf{n}_{\Gamma_c^+} \boldsymbol{\psi} d\Gamma + \oint_{\Gamma_c^-} \mathbf{N}^\top \mathbf{n}_{\Gamma_c^-} \boldsymbol{\psi} d\Gamma \tag{A.25}$$

$$\mathbf{K}_{u\theta} = -\int_\Omega \{\mathbf{B}\}^\top \mathbf{D}\alpha \begin{bmatrix} \mathbf{N} \\ \mathbf{N} \\ \mathbf{N} \\ 0 \\ 0 \\ 0 \end{bmatrix} d\Omega \tag{A.26}$$

$$\mathbf{K}_{pu} = \oint_{\Gamma_c^+} \mathbb{B}^\top \cdot \rho_f \nabla p \frac{\partial w^n k(w^n)}{\partial w^n} \mathbf{n}_{\Gamma_c^+}^\top \mathbf{N} d\Gamma + \oint_{\Gamma_c^-} \mathbb{B}^\top \cdot \rho_f \nabla p \frac{\partial w^n k(w^n)}{\partial w^n} \mathbf{n}_{\Gamma_c^-}^\top \mathbf{N} d\Gamma \tag{A.27}$$

$$\mathbf{K}_{pp} = \oint_{\Gamma_c} \mathbb{B}^\top \rho_f w^n k(w^n) \mathbb{B} d\Gamma \tag{A.28}$$

$$\mathbf{K}_{\theta u} = -\left(\oint_{\Gamma_c^+} \mathbf{N}^\top (\theta^n - T^n) \frac{\partial h}{\partial w^n} \mathbf{n}_{\Gamma_c^+}^\top \mathbf{N} d\Gamma + \oint_{\Gamma_c^-} \mathbf{N}^\top (\theta^n - T^n) \frac{\partial h}{\partial w^n} \mathbf{n}_{\Gamma_c^-}^\top \mathbf{N} d\Gamma \right) \tag{A.29}$$

$$\mathbf{K}_{\theta\theta} = \frac{\mathbf{C}}{\Delta t} - \left(\int_\Omega \mathbf{B}^\top k_s \mathbf{B} d\Omega + \oint_{\Gamma_c^+} \mathbf{N}^\top h(w^n) \mathbf{N} d\Gamma + \oint_{\Gamma_c^-} \mathbf{N}^\top h(w^n) \mathbf{N} d\Gamma \right) \tag{A.30}$$

$$\mathbf{K}_{\theta T} = -\left(-\oint_{\Gamma_c^+} \mathbf{N}^\top h(w^n) \boldsymbol{\psi} d\Gamma - \oint_{\Gamma_c^-} \mathbf{N}^\top h(w^n) \boldsymbol{\psi} d\Gamma \right) \tag{A.31}$$

$$\begin{aligned} \mathbf{K}_{Tu} = & -\oint_{\Gamma_c^+} \boldsymbol{\psi}^\top (\theta^n - T^n) \frac{\partial h}{\partial w^n} \mathbf{n}_{\Gamma_c^+}^\top \mathbf{N} d\Gamma - \oint_{\Gamma_c^-} \boldsymbol{\psi}^\top (\theta^n - T^n) \frac{\partial h}{\partial w^n} \mathbf{n}_{\Gamma_c^-}^\top \mathbf{N} d\Gamma \\ & + \oint_{\Gamma_c^+} \left(\mathbb{B}^\top \cdot k_f \nabla T + \boldsymbol{\psi}^\top \rho_f c_{pf} \nabla T \cdot \frac{\partial (w \boldsymbol{v})}{\partial w^n} \right) \mathbf{n}_{\Gamma_c^+}^\top \mathbf{N} d\Gamma \\ & + \oint_{\Gamma_c^-} \left(\mathbb{B}^\top \cdot k_f \nabla T + \boldsymbol{\psi}^\top \rho_f c_{pf} \nabla T \cdot \frac{\partial (w \boldsymbol{v})}{\partial w^n} \right) \mathbf{n}_{\Gamma_c^-}^\top \mathbf{N} d\Gamma \\ & + \oint_{\Gamma_c^+} \mathbb{B}^\top \rho_f c_{pf} \tau \left(\frac{\partial (w \boldsymbol{v})}{\partial w^n} \Re(T^h) \mathbf{n}_{\Gamma_c^+}^\top \mathbf{N} + w \boldsymbol{v} \frac{\partial \Re(T^h)}{\partial \mathbf{d}} \right) d\Gamma \\ & + \oint_{\Gamma_c^-} \mathbb{B}^\top \rho_f c_{pf} \tau \left(\frac{\partial (w \boldsymbol{v})}{\partial w^n} \Re(T^h) \mathbf{n}_{\Gamma_c^-}^\top \mathbf{N} + w \boldsymbol{v} \frac{\partial \Re(T^h)}{\partial \mathbf{d}} \right) d\Gamma \end{aligned} \tag{A.32}$$

$$\begin{aligned} \mathbf{K}_{Tp} = & \oint_{\Gamma_c} \boldsymbol{\psi}^\top \rho_f c_{pf} \nabla T \cdot (-w k(w^n)) \mathbb{B} d\Gamma \\ & + \oint_{\Gamma_c} \mathbb{B}^\top \rho_f c_{pf} \tau \left(-w k(w^n) \Re(T^h) \mathbb{B} + w \boldsymbol{v} \frac{\partial \Re(T^h)}{\partial \mathbf{p}} \right) d\Gamma \end{aligned} \tag{A.33}$$

$$\mathbf{K}_{T\theta} = -\oint_{\Gamma_c^+} \boldsymbol{\psi}^\top h(w^n)\mathbf{N} d\Gamma - \oint_{\Gamma_c^-} \boldsymbol{\psi}^\top h(w^n)\mathbf{N} d\Gamma + \oint_{\Gamma_c} \mathbb{B}^\top \cdot w\boldsymbol{v}\rho_f c_{pf}\tau \frac{\partial \Re(T^h)}{\partial \boldsymbol{\theta}} d\Gamma \tag{A.34}$$

$$\begin{aligned}\mathbf{K}_{TT} = &-\oint_{\Gamma_c} \left(\mathbb{B}^\top w^n k_f \mathbb{B} + \boldsymbol{\psi}^\top \rho_f c_{pf} w\boldsymbol{v}\cdot\mathbb{B}\right) d\Gamma - 2\oint_{\Gamma_c} \boldsymbol{\psi}^\top h(w^n)\boldsymbol{\psi} d\Gamma \\ &+ \oint_{\Gamma_c} \mathbb{B}^\top \cdot w\boldsymbol{v}\rho_f c_{pf}\tau \frac{\partial \Re(T^h)}{\partial \mathbf{T}} d\Gamma\end{aligned} \tag{A.35}$$

The derivatives of the advection stabilization residual for linear elements with respect to the degrees of freedom are

$$\frac{\partial \Re}{\partial \mathbf{u}} = \left(\frac{\partial w\boldsymbol{v}}{\partial w}\cdot \rho_f c_{pf}\nabla T - \left(\langle\!\langle \theta \rangle\!\rangle - 2T\right)\frac{\partial h}{\partial w}\right)\mathbf{n}_{\Gamma_c}^\top \mathbf{N} \tag{A.36}$$

$$\frac{\partial \Re}{\partial \mathbf{p}} = -wk(w)\rho_f c_{pf}\nabla T \cdot \mathbb{B} \tag{A.37}$$

$$\frac{\partial \Re}{\partial \boldsymbol{\theta}} = -h\mathbf{N} \tag{A.38}$$

$$\frac{\partial \Re}{\partial \mathbf{T}} = w\boldsymbol{v}\cdot\rho_f c_{pf}\mathbb{B} + 2h\boldsymbol{\psi} \tag{A.39}$$

References

[1] Geothermal Energy Resource Potential of Canada, Geological Survey of Canada Open File ; 6914, Geological Survey of Canada, Ottawa, Ont, 2013.

[2] S. Pandey, V. Vishal, A. Chaudhuri, Geothermal reservoir modeling in a coupled thermo-hydro-mechanical-chemical approach: A review, Earth-Sci. Rev. 185 (2018) 1157–1169.

[3] Y.-C. Zeng, Z. Su, N.-Y. Wu, Numerical simulation of heat production potential from hot dry rock by water circulating through two horizontal wells at Desert Peak geothermal field, Energy 56 (2013) 92–107, http://dx.doi.org/10.1016/j.energy.2013.04.055.

[4] M.D. Aliyu, H.-P. Chen, Enhanced geothermal system modelling with multiple pore media: Thermo-hydraulic coupled processes, Energy 165 (2018) 931–948, http://dx.doi.org/10.1016/j.energy.2018.09.129.

[5] G. Wang, G. Liu, Z. Zhao, Y. Liu, H. Pu, A robust numerical method for modeling multiple wells in city-scale geothermal field based on simplified one-dimensional well model, Renew. Energy 139 (2019) 873–894.

[6] A. Ghassemi, X. Zhou, A three-dimensional thermo-poroelastic model for fracture response to injectionextraction in enhanced geothermal systems, Geothermics 40 (1) (2011) 39–49.

[7] Q. Gan, D. Elsworth, Production optimization in fractured geothermal reservoirs by coupled discrete fracture network modeling, Geothermics 62 (2016) 131–142, http://dx.doi.org/10.1016/j.geothermics.2016.04.009.

[8] A.R. Shaik, S.S. Rahman, N.H. Tran, T. Tran, Numerical simulation of fluid-rock coupling heat transfer in naturally fractured geothermal system, Appl. Therm. Eng. 31 (10) (2011) 1600–1606.

[9] Y. Chen, G. Ma, H. Wang, T. Li, Evaluation of geothermal development in fractured hot dry rock based on three dimensional unified pipe-network method, Appl. Therm. Eng. 136 (2018) 219–228.

[10] M. Vasilyeva, M. Babaei, E.T. Chung, D. Spiridonov, Multiscale modeling of heat and mass transfer in fractured media for enhanced geothermal systems applications, Appl. Math. Model. 67 (2019) 159–178.

[11] M. Vasilyeva, M. Babaei, E.T. Chung, V. Alekseev, Upscaling of the single-phase flow and heat transport in fractured geothermal reservoirs using nonlocal multicontinuum method, Comput. Geosci. 23 (4) (2019) 745–759.

[12] M. HosseiniMehr, C. Vuik, H. Hajibeygi, Adaptive dynamic multilevel simulation of fractured geothermal reservoirs, J. Comput. Phys.: X (2020) 100061.

[13] Y. Wang, T. Li, Y. Chen, G. Ma, A three-dimensional thermo-hydro-mechanical coupled model for enhanced geothermal systems (EGS) embedded with discrete fracture networks, Comput. Methods Appl. Mech. Engrg. 356 (2019) 465–489.

[14] W. Zhang, Z. Qu, T. Guo, Z. Wang, Study of the enhanced geothermal system (EGS) heat mining from variably fractured hot dry rock under thermal stress, Renew. Energy 143 (2019) 855–871.

[15] T. Garipov, M. Hui, Discrete fracture modeling approach for simulating coupled thermo-hydro-mechanical effects in fractured reservoirs, Int. J. Rock Mech. Min. Sci. (Oxf. Engl.: 1997) 122 (2019) 104075.

[16] R. Mohais, C. Xu, P. Dowd, Fluid flow and heat transfer within a single horizontal fracture in an enhanced geothermal system, J. Heat Transfer 133 (11) (2011).

[17] Y. Xia, M. Plummer, E. Mattson, R. Podgorney, A. Ghassemi, Design, modeling, and evaluation of a doublet heat extraction model in enhanced geothermal systems, Renew. Energy 105 (2017) 232–247, http://dx.doi.org/10.1016/j.renene.2016.12.064.

[18] B. Guo, P. Fu, Y. Hao, C.A. Peters, C.R. Carrigan, Thermal drawdown-induced flow channeling in a single fracture in EGS, Geothermics 61 (C) (2016) 46–62.

[19] S. Pandey, A. Chaudhuri, S. Kelkar, A coupled thermo-hydro-mechanical modeling of fracture aperture alteration and reservoir deformation during heat extraction from a geothermal reservoir, Geothermics 65 (2017) 17–31.

[20] S. Salimzadeh, A. Paluszny, H.M. Nick, R.W. Zimmerman, A three-dimensional coupled thermo-hydro-mechanical model for deformable fractured geothermal systems, Geothermics 71 (2018) 212–224.
[21] P. Asai, P. Panja, R. Velasco, J. Mclennan, J. Moore, Fluid flow distribution in fractures for a doublet system in Enhanced Geothermal Systems (EGS), Geothermics 75 (C) (2018) 171–179.
[22] S. Han, Y. Cheng, Q. Gao, C. Yan, J. Zhang, Numerical study on heat extraction performance of multistage fracturing Enhanced Geothermal System, Renew. Energy 149 (2020) 1214–1226, http://dx.doi.org/10.1016/j.renene.2019.10.114.
[23] F. Gong, T. Guo, W. Sun, Z. Li, B. Yang, Y. Chen, Z. Qu, Evaluation of geothermal energy extraction in Enhanced Geothermal System (EGS) with multiple fracturing horizontal wells (MFHW), Renew. Energy 151 (2020) 1339–1351, http://dx.doi.org/10.1016/j.renene.2019.11.134.
[24] H. Slatlem Vik, S. Salimzadeh, H.M. Nick, Heat recovery from multiple-fracture enhanced geothermal systems: The effect of thermoelastic fracture interactions, Renew. Energy 121 (2018) 606–622.
[25] S. Salimzadeh, H.M. Nick, R. Zimmerman, Thermoporoelastic effects during heat extraction from low-permeability reservoirs, Energy 142 (2018) 546–558.
[26] S. Salimzadeh, H. Nick, A coupled model for reactive flow through deformable fractures in Enhanced Geothermal Systems, Geothermics 81 (2019) 88–100.
[27] M. Parchei Esfahani, R. Gracie, On the undrained and drained hydraulic fracture splits, Internat. J. Numer. Methods Engrg. 118 (12) (2019) 741–763.
[28] E. Gordeliy, A. Peirce, Enrichment strategies and convergence properties of the XFEM for hydraulic fracture problems, Comput. Methods Appl. Mech. Engrg. 283 (C) (2015) 474–502.
[29] J. Kim, H. Tchelepi, R. Juanes, Stability and convergence of sequential methods for coupled flow and geomechanics: Fixed-stress and fixed-strain splits, Comput. Methods Appl. Mech. Engrg. 200 (13–16) (2011) 1591–1606.
[30] J. Kim, H. Tchelepi, R. Juanes, Stability and convergence of sequential methods for coupled flow and geomechanics: Drained and undrained splits, Comput. Methods Appl. Mech. Engrg. 200 (23–24) (2011) 2094–2116.
[31] A. Mikelić, M. Wheeler, Convergence of iterative coupling for coupled flow and geomechanics, Comput. Geosci. 17 (3) (2013) 455–461.
[32] U. S. D. of Energy, Utah FORGE numerical modelling, 2020, https://utahforge.com/laboratory/numerical-modeling. Accessed 2020-06-10. URL https://utahforge.com/laboratory/numerical-modeling.
[33] A. Bejan, Convection Heat Transfer, fourth ed., Wiley, Hoboken, N.J., 2013.
[34] I. Harari, Stability of semidiscrete formulations for parabolic problems at small time steps, Comput. Methods Appl. Mech. Engrg. 193 (15–16) (2004) 1491–1516.
[35] I. Faragó, R. Horváth, A review of reliable numerical models for three-dimensional linear parabolic problems, Internat. J. Numer. Methods Engrg. 70 (1) (2007) 25–45.
[36] C.J. van Duijn, A. Mikelić, T. Wick, Mathematical theory and simulations of thermoporoelasticity, Comput. Methods Appl. Mech. Engrg. 366 (2020) 113048.
[37] A.N. Brooks, T.J. Hughes, Streamline upwind/Petrov-Galerkin formulations for convection dominated flows with particular emphasis on the incompressible Navier-Stokes equations, Comput. Methods Appl. Mech. Engrg. 32 (1–3) (1982) 199–259.
[38] F. Shakib, T.J. Hughes, Z. Johan, A new finite element formulation for computational fluid dynamics: X. The compressible Euler and Navier-Stokes equations, Comput. Methods Appl. Mech. Engrg. 89 (1–3) (1991) 141–219.
[39] U. Küttler, W. Wall, Fixed-point fluid–structure interaction solvers with dynamic relaxation, Comput. Mech. 43 (1) (2008) 61–72.
[40] R. Schussnig, T. Peter, Fluid-structure interaction in aortic dissection - A monolithic approach, 2019, ECCOMAS Young Investigators Conference ; Conference date: 01-09-2019 Through 06-09-2019.
[41] O.C. Zienkiewicz, J.Z. Zhu, The superconvergent patch recovery and a posteriori error estimates. Part 1: The recovery technique, Internat. J. Numer. Methods Engrg. 33 (7) (1992) 1331–1364.
[42] W.H. Somerton, Thermal Properties and Temperature-Related Behavior of Rock/fluid Systems, in: Developments in Petroleum Science, vol. 37, Elsevier, Amsterdam, 1992.
[43] O. Kolditz, U.-J. Görke, H. Shao, W. Wang, Thermo-Hydro-Mechanical-Chemical Processes in Porous Media: Benchmarks and Examples, in: Lecture Notes in Computational Science and Engineering, vol. 86, Springer Berlin Heidelberg, Berlin, Heidelberg, 2012.
[44] F. Heuze, High-temperature mechanical, physical and thermal properties of granitic rocks— a review, Int. J. Rock Mech. Min. Sci. Geomech. Abstr. 20 (1) (1983) 3–10.
[45] S.D. Walsh, N. Garapati, A.M. Leal, M.O. Saar, Calculating thermophysical fluid properties during geothermal energy production with NESS and reaktoro, Geothermics 70 (2017) 146–154.